Research article

Accelerated phosphatidylcholine turnover in macrophages promotes adipose tissue inflammation in obesity

Authors

Kasparas Petkevicius[1], Samuel Virtue[1], Guillaume Bidault[1], Benjamin Jenkins[1], Cankut Çubuk[3,4,5], Cecilia Morgantini[6], Myriam Aouadi[6], Joaquin Dopazo[3,4,5], Mireille Serlie[7], Albert Koulman[1], and Antonio Vidal-Puig[1,2]

Affiliations

[1]University of Cambridge Metabolic Research Laboratories, Institute of Metabolic Science, MDU MRC. Addenbrooke's Hospital, Cambridge, CB2 0QQ, UK

[2]Wellcome Trust Sanger Institute, Hinxton CB10 1SA, UK

[3]Clinical Bioinformatics Area, Fundación Progreso y Salud, CDCA, Hospital Virgen del Rocio, Sevilla, Spain

[4]Functional Genomics Node, INB-ELIXIR-es, FPS, Hospital Virgen del Rocio, Sevilla, Spain

[5]Bioinformatics in Rare Diseases (BiER), Centro de Investigación Biomédica en Red de Enfermedades Raras (CIBERER), FPS, Hospital Virgen del Rocio, Sevilla, Spain

[6]Integrated Cardio Metabolic Centre, Department of Medicine, Karolinska Institutet, Blickagången 6, 141 57 Huddinge, Sweden

[7]Department of Endocrinology and Metabolism, Amsterdam University Medical Center, F5-167, Meibergdreef 9, 1105 AZ, Amsterdam, Netherlands

Abstract

White adipose tissue (WAT) inflammation contributes to the development of insulin resistance in obesity. While the role of adipose tissue macrophage (ATM) pro-inflammatory signalling in the development of insulin resistance has been established, it is less clear how WAT inflammation is initiated. Here, we show that ATMs from obese mice and humans exhibit markers of increased *de novo* phosphatidylcholine (PC) biosynthesis rate. Macrophage-specific knockout of phosphocholine-cytidylyltransferase A (CCTα), the rate-limiting enzyme of *de novo* PC biosynthesis pathway, alleviated obesity-induced WAT inflammation and insulin resistance. Mechanistically, CCTα-deficient macrophages showed reduced ER stress and inflammation in response to palmitate. Surprisingly, this was not due to lower exogenous palmitate incorporation into cellular PCs. Instead, CCTα-null macrophages had lower PC turnover, leading to elevated membrane polyunsaturated fatty acids that negated the pro-inflammatory effects of palmitate. Our results reveal a link between obesity-associated increase in PC synthesis, accelerated PC turnover and pro-inflammatory activation of ATMs.

Introduction

Obesity-related metabolic disorders are among the most prevalent causes of death worldwide. Secondary complications of obesity have been suggested to be caused by the functional failure of white adipose tissue (WAT), leading to ectopic lipid deposition, lipotoxicity and systemic insulin resistance (Virtue and Vidal-Puig, 2010). Obesity is associated with a chronic low-grade inflammation, characterised by immune cell infiltration to WAT, a switch of adipose tissue macrophage (ATM) polarisation from a tissue-remodelling (M2) to a pro-inflammatory (M1) state and elevated production of pro-inflammatory, insulin-desensitising cytokines, such as tumour necrosis factor α (TNFα). Over the last decade, multiple genetic and pharmacological approaches have defined a causal role of macrophage-driven WAT inflammation in the development of insulin resistance (Hotamisligil, 2017). However, specific pathophysiological mechanisms triggering pro-inflammatory activation of ATMs during obesity are poorly understood.

Our previous work identified that the lipid composition of ATMs undergoes both quantitative and qualitative changes during obesity (Prieur et al., 2011). Qualitative changes in the lipid composition of both plasma and endoplasmic reticulum (ER) membranes represent a major factor promoting insulin resistance (Fu et al., 2011; Holzer et al., 2011; Wei et al., 2016). Obesity-associated alterations in ER lipid composition lead to a cellular process termed ER stress, which invokes an adaptive unfolded protein response (UPR) (Hou et al., 2014). In macrophages, the UPR is coupled to the activation of intracellular inflammatory signalling pathways that cause WAT inflammation and insulin resistance (Robblee et al., 2016; Shan et al., 2017; Suzuki et al., 2017). Furthermore, M1 macrophages are characterised by increased

endogenous fatty acid synthesis, which stabilises lipid rafts within plasma membrane to allow pro-inflammatory signal transduction in obesity (Wei et al., 2016). While phospholipids (PLs) are the main constituents of plasma and ER membranes, the importance of PL biosynthesis in ATMs during obesity has not yet been investigated.

The concept that macrophage ER stress could be induced during obesity due to changes in membrane composition is in line with the known physiological changes in lipid metabolism that occur during obesity. Obesity is associated with increased circulating saturated fatty acids (SFAs), which cause cellular ER stress by being incorporated into membrane PLs, leading to a decreased membrane fluidity due to increased membrane PL acyl chain saturation. Increased SFA-mediated ER rigidification is directly sensed by the transmembrane domains of UPR-transducing proteins (Robblee et al., 2016; Volmer et al., 2013). ER fatty acid saturation and the resulting UPR can be counteracted by both endogenously and exogenously derived mono- and polyunsaturated fatty acids (MUFAs and PUFAs), and PUFA-containing phospholipids, in particular phosphatidylcholines (PCs) (Ariyama et al., 2010; Gianfrancesco et al., 2019; Robblee et al., 2016; Rong et al., 2013).

PC is the most abundant PL in mammalian cells. Most cells can synthesise PC *de novo* through the Kennedy pathway, involving the transfer of phosphocholine onto diacylglycerol moiety. PCs synthesised *de novo* predominantly contain saturated (SFAs) and monounsaturated fatty acids (MUFAs), while polyunsaturated fatty acids (PUFAs) are incorporated into PCs via the Lands cycle, involving a hydrolysis of a single fatty acyl chain and esterification of a free PUFA to a resulting lysophosphatidylcholine (lysoPC) (Shindou et al., 2013). Metabolic flux through the *de*

novo PC synthesis pathway and cellular PC levels are greatly increased in differentiating macrophages (Ecker et al., 2010). Furthermore, pro-inflammatory signalling via toll-like receptor 4 (TLR4) increases the rate of choline uptake and *de novo* PC synthesis in macrophages (Sanchez-Lopez et al., 2019; Snider et al., 2018; Tian et al., 2008). However, *de novo* PC synthesis in mature macrophages is not coupled to the expansion of the cellular PC pool, as it is counteracted by phospholipase D activity, leading to a rapid turnover of membrane PCs (Jackowski et al., 1997). The consequences of altered PC turnover in metabolic disease are not currently known.

Conceptually, the rate of *de novo* PC synthesis and turnover should affect PC remodelling via Lands cycle. The role of the Lands cycle in ER stress function has been studied by genetic manipulation of the enzyme lysoPC-acyltransferase 3 (LPCAT3), the major LPCAT isoform in macrophages (Jiang et al., 2018). LPCAT3 overexpression increases the rate of PUFA incorporation into PCs and protects cells from palmitate-induced ER stress, while the loss of LPCAT3 sensitises cells to palmitate lipotoxicity (Rong et al., 2013).

We have previously shown that during obesity, ATMs acquire an M1 phenotype concomitantly with their intracellular lipid accumulation (Prieur et al., 2011). Here, we demonstrate that markers of *de novo* PC synthesis are increased in ATMs isolated from obese mice and humans. Ob/ob mice with a myeloid cell-specific reduction in *de novo* PC synthesis rate display reduced adipose tissue inflammation and improved metabolic profile compared to controls. Mechanistically, we show that reducing the activity of the *de novo* PC synthesis pathway by 30% does not reduce total cellular PC

levels in macrophages. Instead, the reduction in PC synthesis is balanced by a reduction in PC degradation, maintaining the cellular PC pool size but increasing the half-life of PCs. The extended PC half-life leads to increased incorporation of PUFAs into PCs by allowing more time for PC remodelling. Elevated PC PUFA content protects macrophages from palmitate-induced ER stress and pro-inflammatory activation.

Results

Obesity accelerates *de novo* PC biosynthesis in ATMs

In order to identify intrinsic metabolic pathways associated with the phenotypic switch of ATMs towards an M1 polarisation state, we reanalysed our published microarray dataset (GSE36669) of epididymal WAT (eWAT) macrophages isolated from WT and ob/ob animals using inferred metabolic flux analysis (Cubuk et al., 2018a; 2018b). We focused on the pathways that were unchanged or downregulated in 5-week-old ob/ob ATMs, which are predominantly M2-polarised, but upregulated at 16 weeks of age, when eWAT of ob/ob mice is inflamed (Prieur et al., 2011). Among the metabolic pathways that fitted these criteria was *de novo* PC biosynthesis (Figure 1a-b), with a lower inferred activity score in 5-week-old, but higher score in 16-week-old ob/ob ATMs compared to age-matched WT controls (Figure 1d). Further analysis of the processes that were unchanged at 5 weeks but upregulated at 16 weeks in ob/ob ATMs revealed several pathways related to PL metabolism (Figure 1d, Table S1). The activity of *de novo* PE biosynthesis pathway was not modulated in ob/ob ATMs (Figure 1-figure supplement 1a-b).

We next determined whether increased inferred activity of the *de novo* PC synthesis pathway in obesity was specific to ATMs, or also occurred in other tissue-resident macrophages. We performed global transcriptomic comparison between liver macrophages isolated from 14-week-old ob/ob and control mice. Unlike ATMs, liver macrophages isolated from obese mice showed similar expression levels of *de novo* PC biosynthesis pathway constituents compared to controls (Figure 1-figure supplement 2).

In accordance with our ATM transcriptomic analysis, the expression of *Pcyt1a*, encoding phosphocholine cytidylyltransferase A (CCTα), the rate-limiting enzyme in *de novo* PC synthesis pathway, was unchanged at 5 weeks, but increased at 16 weeks in ob/ob ATMs compared to WT controls when measured by qPCR (Figure 1e). In contrast, the *Pcyt1a* paralogue *Pcyt1b* was down-regulated at 5 weeks and not modulated at 16 weeks in ob/ob ATMs (Figure 1-figure supplement 1c). Furthermore, *Pcyt1a* expression in macrophages isolated from the WAT of obese individuals was positively correlated with BMI (Figure 1f). Of note, out of all analysed tissue macrophage populations publicly available in Immgen database (Heng et al., 2008), ATMs had the highest expression of *Pcyt1a* transcript (Figure 1-figure supplement 3).

We then reanalysed our previously published lipid profiles from ob/ob ATMs (Prieur et al., 2011), focusing only on measured PL species. Relative to the total PL amount, both PC abundance and PC:PE molar ratio tended to increase (Figure 1-figure supplement 4a-b), and palmitate- and stearate-containing lysoPC species were upregulated in 16-week-old ob/ob ATMs compared to WT controls (Figure 1g). It has been previously shown that hepatic lysoPC levels are reduced when the balance between PC synthesis and LPCAT activity is perturbed. Specifically, increasing LPCAT3 activity without changing *de novo* PC synthesis or breakdown reduces LysoPC levels, as LPCAT3 re-esterifies LysoPC into PC (Rong et al., 2013). Conversely, in obese WAT, despite the upregulation of *Lpcat3* transcript at both 5 and 16 weeks in ob/ob ATMs (Figure 1-figure supplement 5a), we observed increased lysoPC species in ob/ob ATMs (Figure 1g). The elevation in LysoPCs was therefore consistent with obesity causing a disproportional increase in the rate of both *de novo*

PC synthesis and hydrolysis that exceeded the capacity of LPCAT3 to re-esterify Lyso-PC back into PC (Figure 1-figure supplement 5b).

Figure 1 with 5 supplements

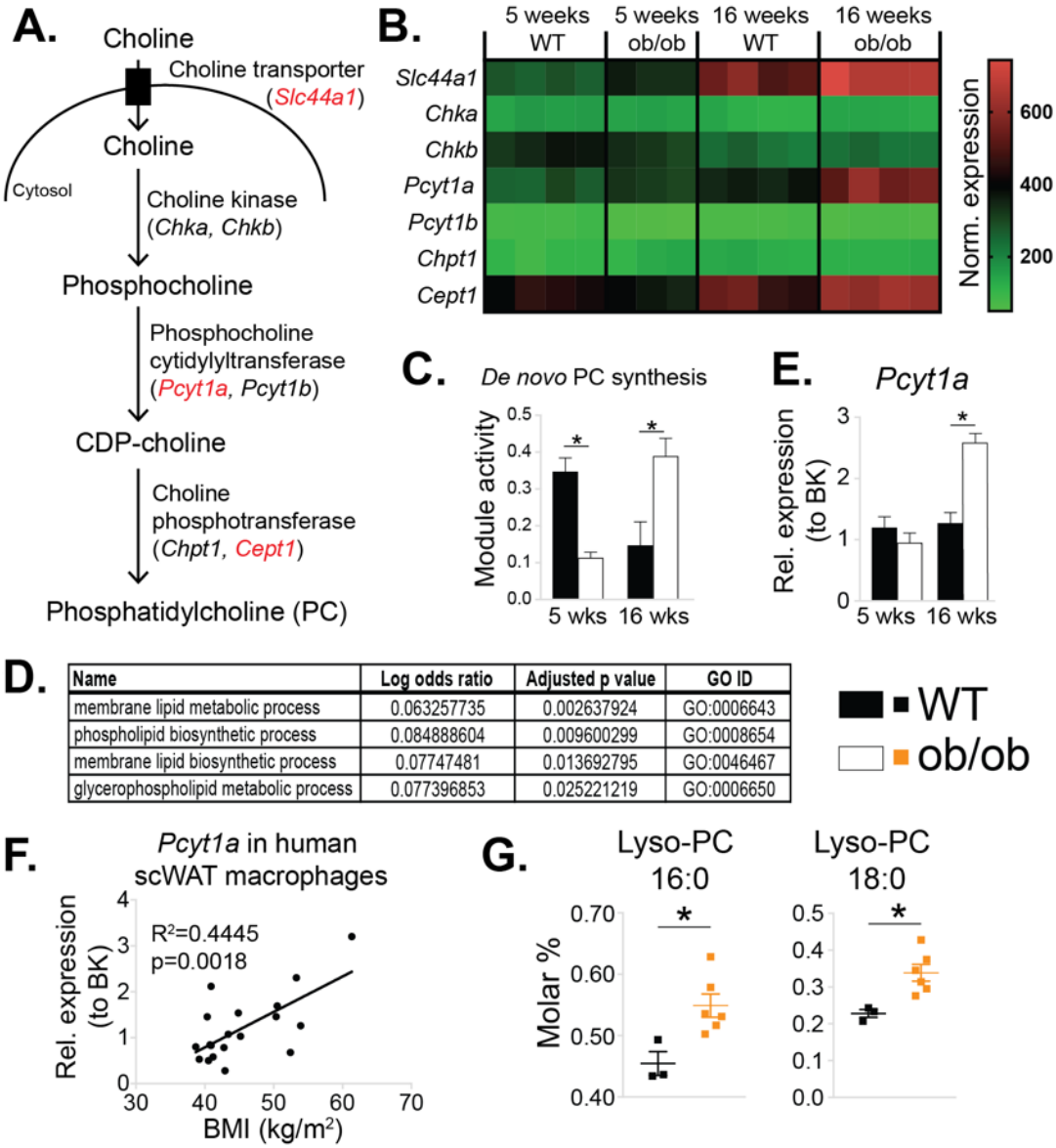

Name	Log odds ratio	Adjusted p value	GO ID
membrane lipid metabolic process	0.063257735	0.002637924	GO:0006643
phospholipid biosynthetic process	0.084888604	0.009600299	GO:0008654
membrane lipid biosynthetic process	0.07747481	0.013692795	GO:0046467
glycerophospholipid metabolic process	0.077396853	0.025221219	GO:0006650

***De novo* PC synthesis rate is increased in ATMs during obesity.**
(A) Simplified schema of the Kennedy pathway of *de novo* PC biosynthesis. Transcripts in red are upregulated in 16-week-old ob/ob eWAT macrophages compared to WT controls.
(B) Normalised microarray gene expression values for the enzymes of the Kennedy pathway of *de novo* PC biosynthesis in eWAT macrophages. Each presented replicate corresponds to a pool of cells isolated from 5 animals.
(C) *De novo* PC biosynthesis pathway module (M00090) activity in eWAT macrophages, as inferred by the Metabolizer algorithm.
(D) Gene Ontology (GO) pathways related to membrane lipid metabolism that are increased in ob/ob eWAT macrophages at 16 weeks, but not at 5 weeks of age compared to WT controls.
(E) *Pcyt1a* expression in eWAT macrophages, measured by qPCR.
(F) *Pcyt1a* expression, measured by qPCR in subcutaneous WAT macrophages isolated from obese patients undergoing bariatric surgery, plotted against their body weight (n=19).

(G) Molar abundance of 16:0 and 18:0 lyso-PC species (expressed as percentage of total measured PLs) in eWAT macrophages (n=3 pools of 5 WT, n=6 ob/ob mice).
∗p < 0.05 between genotypes, error bars indicate SEM.

Figure 1-figure supplement 1

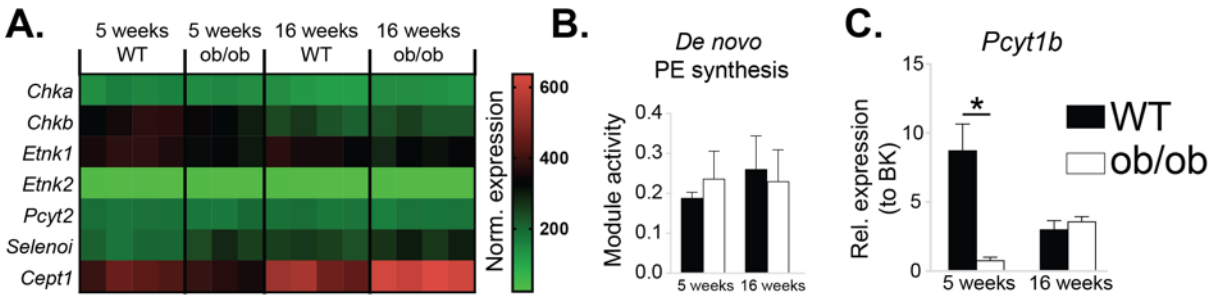

Obesity does not affect *de novo* PE synthesis rate in ATMs.
(A) Normalised microarray gene expression for the enzymes of the Kennedy pathway of *de novo* PE biosynthesis in eWAT macrophages.
(B) *De novo* PE biosynthesis pathway module (M00092) activity in eWAT macrophages, as inferred by the Metabolizer algorithm.
(C) *Pcyt1b* expression in eWAT macrophages, measured by qPCR.
∗p < 0.05 between genotypes, error bars indicate SEM.

Figure 1-figure supplement 2

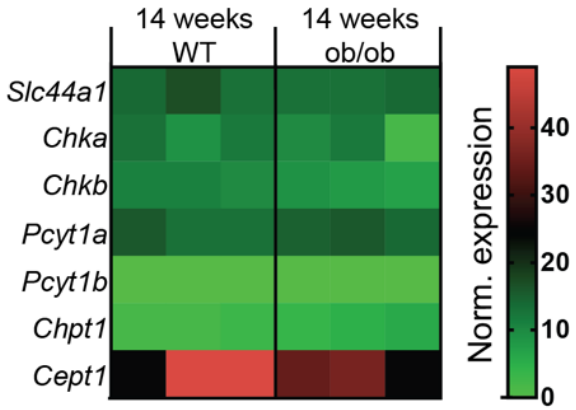

Obesity does not affect *de novo* PC synthesis rate in liver macrophages.
Normalised RNAseq gene expression for the enzymes of the Kennedy pathway of *de novo* PC biosynthesis in liver macrophages, isolated from 14-week-old WT and ob/ob mice (n=3).

Figure 1-figure supplement 3

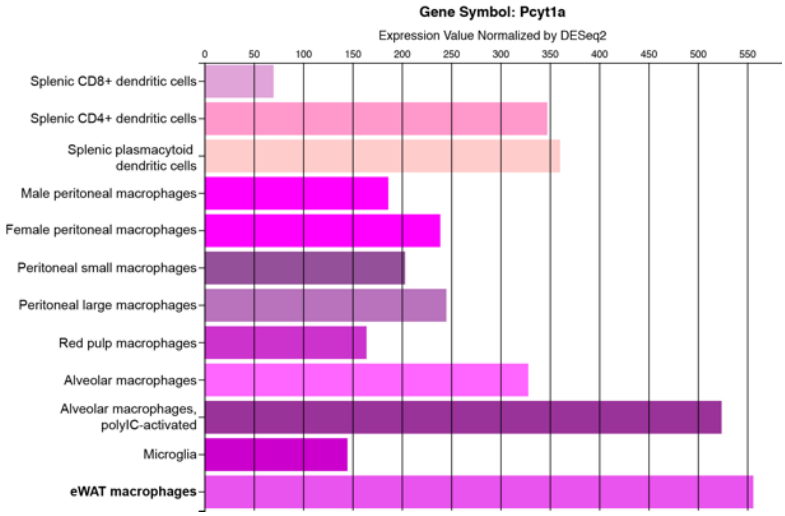

***Pcyt1a* expression levels in different tissue macrophage populations.**

Figure indicating *Pcyt1a* mRNA levels in isolated tissue macrophage populations, measured by RNAseq was obtained directly from Immgen database (www.immgen.org).

Figure 1-figure supplement 4

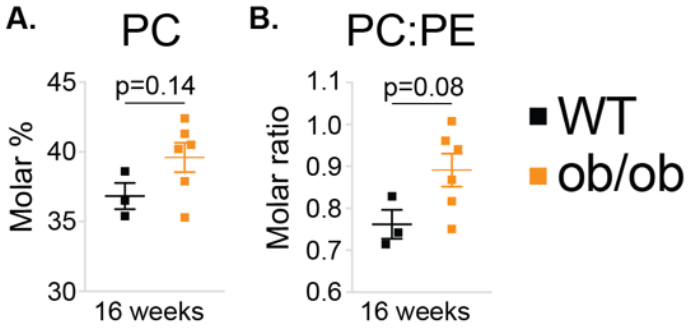

Obesity tends to increase PC molar percentage and PC to PE molar ratio in ATMs.

(A) PC molar abundance (expressed as percentage of total measured PLs), and (B) PC:PE molar ratio in eWAT macrophages (n=3 pools of 5 WT, n=6 16-week-old ob/ob mice). Error bars indicate SEM.

Figure 1-figure supplement 5

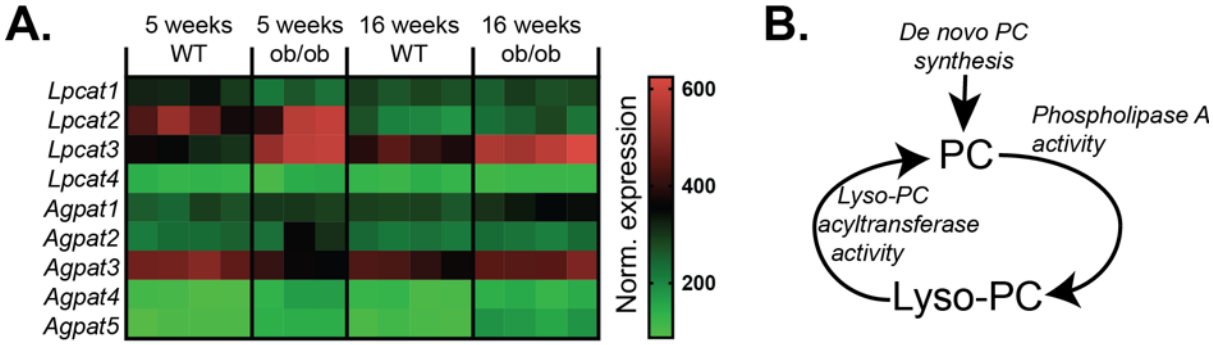

The effects of obesity on PC remodelling gene expression in ATMs.

(A) Normalised microarray gene expression for the enzymes involved in PC remodelling in eWAT macrophages.

(B) Simplified schema of the interaction between *de novo* PC synthesis and PC remodelling pathways.

Pcyt1a deletion in myeloid cells improves glucose metabolism in obese mice

To test if increased PC biosynthesis in ATMs affected whole-organism metabolic homeostasis, we investigated mice with *Pcyt1a* deletion in myeloid cells (CCTα mKO) that have been described previously (Tian et al., 2008). Initially, we sought to validate whether the loss of *Pcyt1a* would impact macrophage differentiation or function *in vitro* and *in vivo*. As indicated by the normal surface expression of macrophage markers F4/80, CD206 and CD301, unaltered bacterial phagocytosis and normal TNFα and IL-6 cytokine secretion in response to LPS, the differentiation of CCTα-null bone marrow cells into macrophages (BMDMs) was not impaired (Figure 2-figure supplement 1a-c). *Pcyt1a* transcript levels in BMDMs on a C57Bl6/J genetic background were reduced by ~50%, which translated into ~80% decrease in CCTα protein expression and ~30% decrease in *de novo* PC synthesis rate compared to controls (Figure 2-figure supplement 1d). *In vivo*, the expression of macrophage mRNA markers in eWAT and liver was comparable between CCTα mKO and control animals (Figure 2-figure supplement 2a-b). Overall, these results confirmed that loss of *Pcyt1a* reduced *de novo* PC biosynthesis rate in macrophages without altering their development or function.

CCTα mKO mice exhibited similar growth rates and metabolic tissue weights compared to controls (Figure 2-figure supplement 3a-b). No differences in glucose or insulin tolerance tests were observed between CCTα mKO and control groups (Figure 2-figure supplement 3c-d). In accordance, the expression levels of insulin-regulated metabolic genes were similar in eWAT and liver of CCTα mKO and control mice (Figure 2-figure supplement 2a-b).

We next evaluated the importance of increased macrophage *de novo* PC synthesis in obesity. We first confirmed that bone marrow transplantation did not alter the induction of *Pcyt1a* in the ob/ob genetic background (Figure 2-figure supplement 4). We then transplanted CCTα mKO or control bone marrow into irradiated ob/ob animals (Figure 2a). While no differences in post-irradiation body weight gain, WAT and liver mass were observed (Figure 2b-c), ob/ob mice carrying CCTα mKO bone marrow tended to have improved glucose tolerance and exhibited increased sensitivity to exogenous insulin compared to controls (Figure 2d-e). Overall, macrophage-specific *Pcyt1a* deletion did not affect ATM development, adipose tissue function and glucose metabolism in lean animals, but improved systemic glucose handling in ob/ob mice, the model of obesity in which we originally observed an induction of *Pcyt1a* in the ATM population.

Figure 2 with 4 supplements

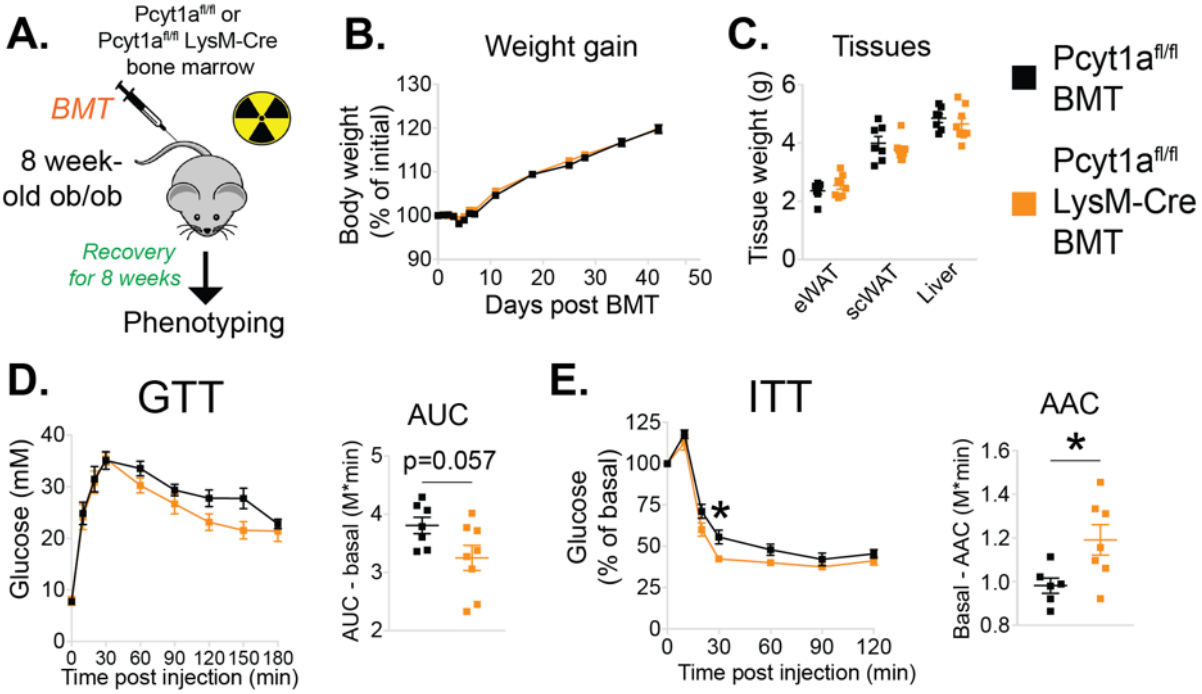

Myeloid cell-specific deletion of *Pcyt1a* leads to improved systemic glucose metabolism on the ob/ob genetic background.
(A) Schema of the BMT study design.
(B) Body weight gain curves and (C) weights of indicated tissues of ob/ob mice transplanted with Pcyt1a$^{fl/fl}$ (n=7) or Pcyt1a$^{fl/fl}$ LysM-Cre (n=8) bone marrow.
(D) GTT curves and areas under curve (AUC), normalised to basal glucose levels.
(E) ITT curves, presented as percentage values of basal glucose levels, and areas above curve (AAC), normalised to basal glucose levels.
∗p < 0.05 between genotypes, error bars indicate SEM.

Figure 2-figure supplement 1

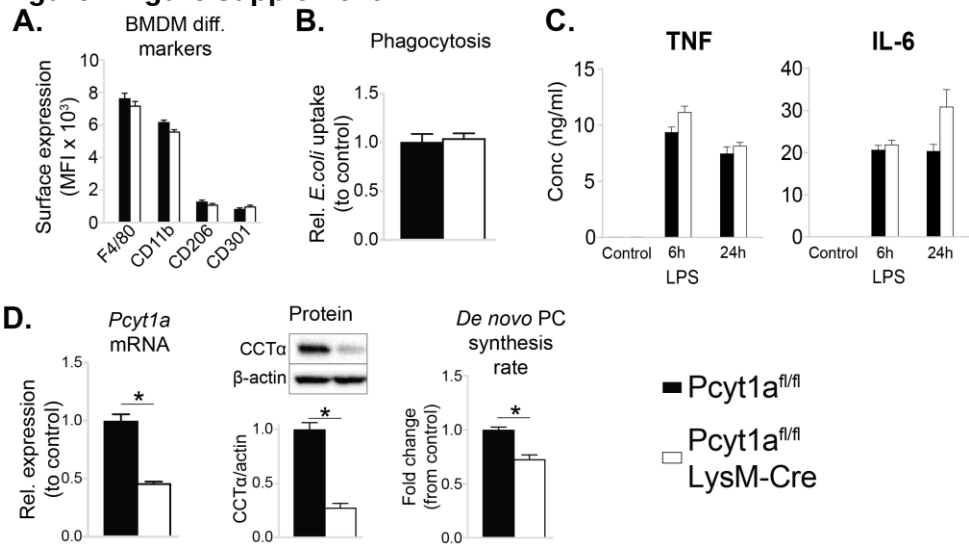

Myeloid cell-specific deletion of *Pcyt1a* does not impair BMDM differentiation or function *in vitro*.
(A) Flow cytometry quantification of macrophage differentiation markers.
(B) Phagocytosis of *E. coli* (normalised to control values).
(C) Cytokine secretion into the medium of BMDMs stimulated with LPS for 6 or 24 hours.
(D) *Pcyt1a* expression, CCTα protein levels and ^{3}H-choline incorporation rate into membrane lipids.

Pcyt1a$^{fl/fl}$ (n=4) or Pcyt1a$^{fl/fl}$ LysM-Cre (n=4) BMDMs in all experiments. ∗p < 0.05 between genotypes, error bars indicate SEM.

Figure 2-figure supplement 2

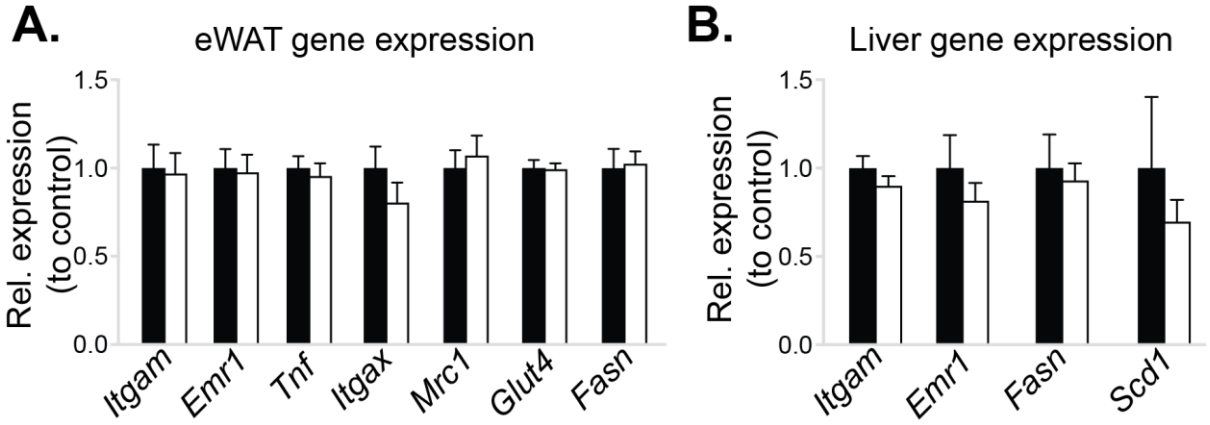

Myeloid cell-specific deletion of *Pcyt1a* does not affect eWAT or liver gene expression in lean mice.
Normalised expression of indicated genes in (A) eWAT and (B) liver of Pcyt1a$^{fl/fl}$ (n=7) or Pcyt1a$^{fl/fl}$ LysM-Cre (n=9) animals on a C57Bl/6J genetic background, measured by qPCR. Error bars indicate SEM.

Figure 2-figure supplement 3

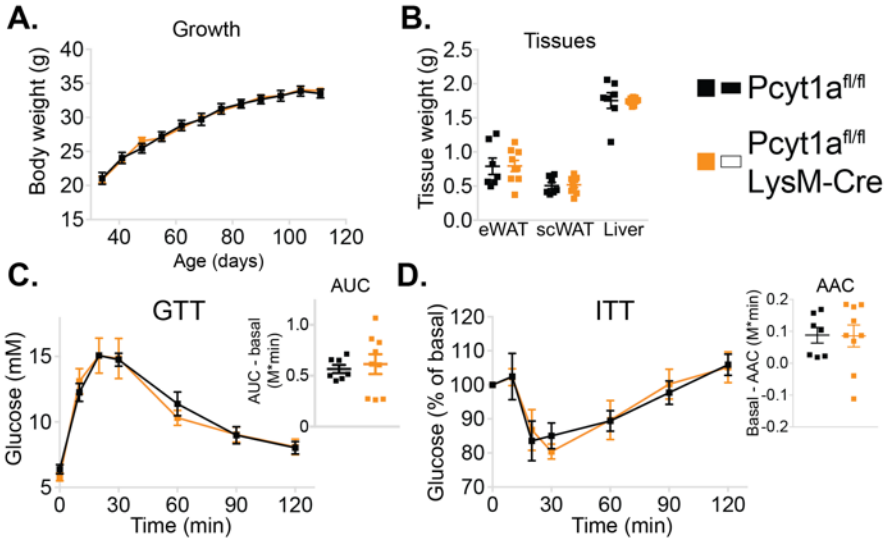

Myeloid cell-specific deletion of *Pcyt1a* does not affect growth or glucose metabolism of lean mice.
(A) Body weight gain curves and (B) tissue weights of lean mice.
(C) GTT curves and areas under curve (AUC), normalised to basal glucose levels.
(D) ITT curves, presented as percentage values of basal glucose levels, and areas above curve (AAC), normalised to basal glucose levels. Error bars indicate SEM.

Figure 2-figure supplement 4

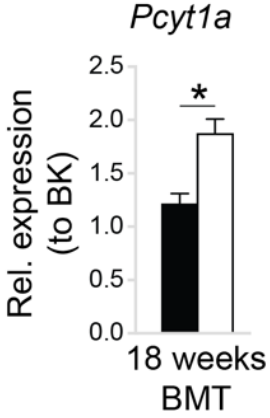

WT to ob/ob bone marrow transplant does not affect the increase of *Pcyt1a* transcription in eWAT ATMs.

Pcyt1a expression measured by qPCR in eWAT macrophages isolated from WT and ob/ob mice carrying WT bone marrow at 18 weeks of age (n=7 mice/group). ∗p < 0.05 between genotypes, error bars indicate SEM.

***Pcyt1a* deletion in myeloid cells alleviates inflammation and improves insulin signalling in the WAT of obese mice**

While the metabolic effects of macrophage-specific *Pcyt1a* deletion on an ob/ob background were modest, they were consistent with the relatively small reduction (30%) in *de novo* PC biosynthesis rate we observed in BMDMs *in vitro*. We next sought to determine how *Pcyt1a* deficiency in macrophages improved glucose metabolism in obese mice. First, we performed whole transcriptome comparison of eWAT isolated from CCTα mKO ob/ob BMT and control animals. Pathway analysis of the transcriptomic data revealed an increase in transcripts associated with insulin sensitivity and glucose metabolism, while pathways related to ER stress and macrophage-driven inflammation were supressed in CCTα mKO compared to control BMT ob/ob mice (Figure 3a, Table S2). RNA sequencing results were also confirmed by qPCR (Figure 2-figure supplement 1a). In accordance to the gene expression data, insulin-responsive AKT phosphorylation was increased in the eWAT of CCTα mKO ob/ob animals compared to controls (Figure 3b-c). Furthermore, while we found no differences in total ATM number, eWAT macrophages showed a shift from M1 to M2 polarisation in CCTα mKO compared to controls (Figure 3d). No differences in the number of crown-like structures (CLS) and eWAT adipocyte area were observed between genotypes (Figure 3-figure supplement 2a-c). Finally, unlike eWAT, the expression of pro-inflammatory and insulin-responsive marker genes in the liver were similar between genotypes (Figure 2-figure supplement 1b). Altogether, we have found that reducing *de novo* PC biosynthesis rate in macrophages alleviates WAT inflammation and insulin resistance in obese mice, without affecting total ATM and CLS number.

Figure 3 with 2 supplements

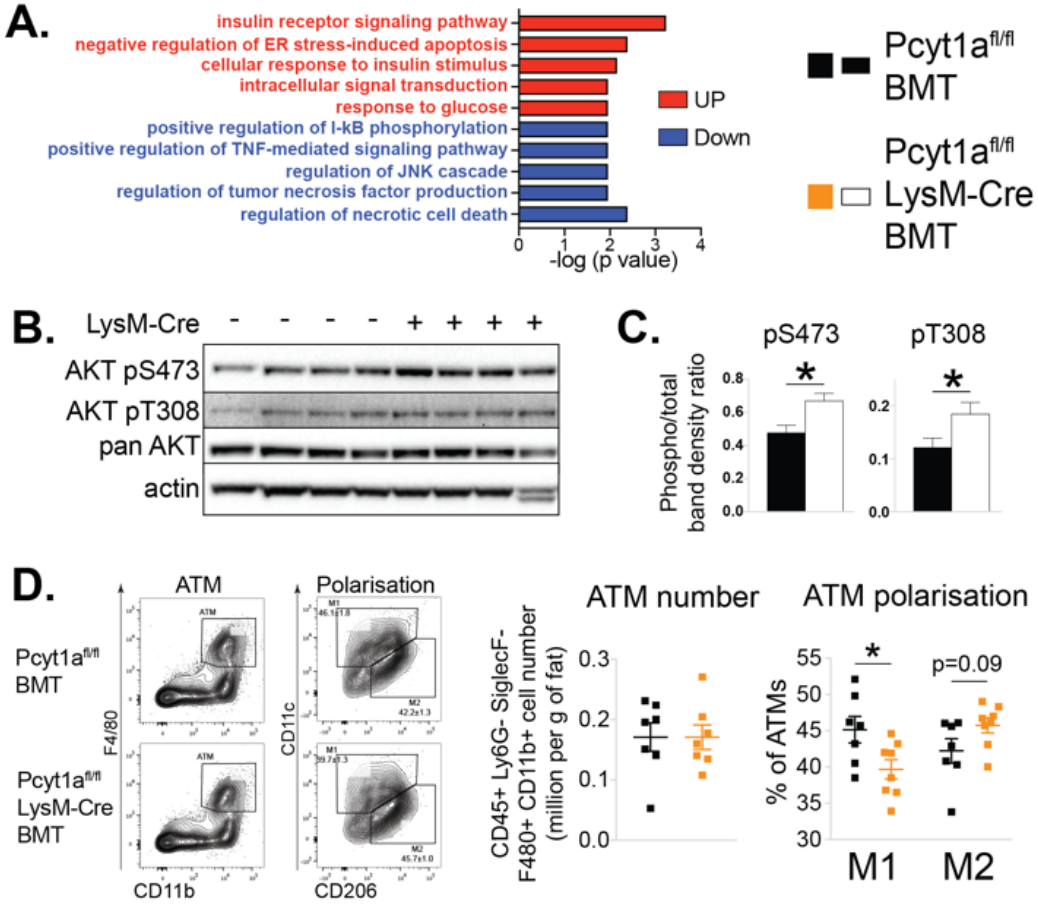

Myeloid cell-specific deletion of *Pcyt1a* leads to reduced WAT inflammation on the ob/ob genetic background.

(A) Selected pathways from eWAT RNAseq analysis, upregulated (red) or downregulated (blue) in ob/ob mice transplanted with Pcyt1a$^{fl/fl}$ LysM-Cre (n=8) bone marrow compared to controls (n=7).
(B) Representative AKT phosphorylation Western blots and (C) their densitometry quantification in eWAT of ob/ob mice transplanted with Pcyt1a$^{fl/fl}$ (n=7) or Pcyt1a$^{fl/fl}$ LysM-Cre (n=8) bone marrow.
(D) Flow cytometry gating strategy, quantification of ATM number per gram of eWAT and the relative polarisation of ATM population in ob/ob mice.
∗p < 0.05 between genotypes, error bars indicate SEM.

Figure 3-figure supplement 1

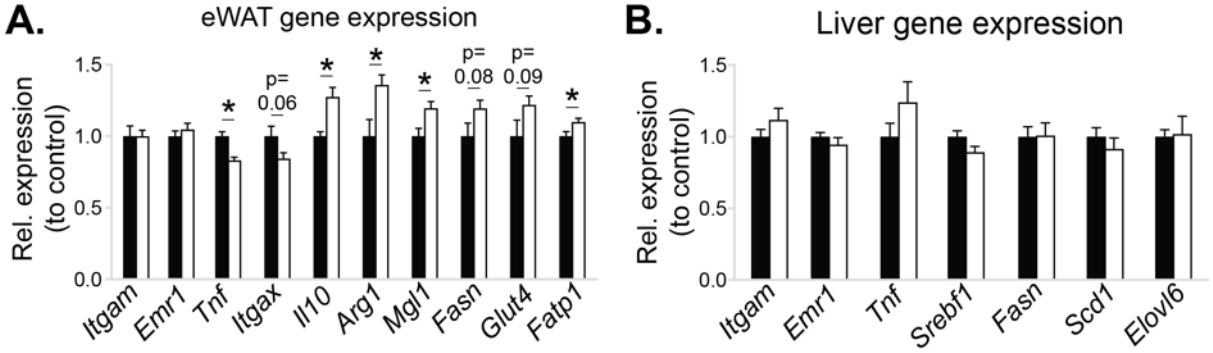

The effects of myeloid cell-specific deletion of *Pcyt1a* on eWAT and liver gene expression on the ob/ob genetic background.

Relative expression of indicated genes in the (A) eWAT and (B) liver of ob/ob BMT mice, measured by qPCR. ∗p < 0.05 between genotypes, error bars indicate SEM.

Figure 3-figure supplement 2

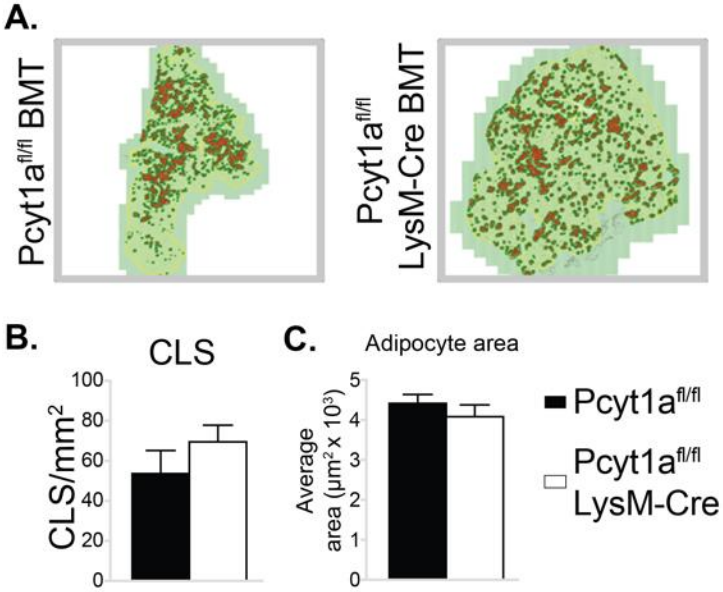

Myeloid cell-specific deletion of *Pcyt1a* does not affect eWAT CLS number or adipocyte size on the ob/ob genetic background.

(A) Representative histology images of eWAT sections of ob/ob BMT mice, CLS are marked in red. Quantification of (B) CLS and (C) average adipocyte area in the eWAT sections of ob/ob BMT mice. Error bars indicate SEM.

Loss of *Pcyt1a* lowers palmitate-induced ER stress and inflammation in macrophages

Next, we sought to investigate the molecular events that reduce WAT inflammation in obese animals carrying CCTα mKO bone marrow. For this purpose, we utilised an *in vitro* model of BMDMs exposed to high palmitate concentrations. We selected palmitate concentrations that have previously been reported to induce ER stress and pro-inflammatory activation, thus mimicking the effects of obesity on ATMs (Robblee et al., 2016). We observed diminished *Tnf* transcript levels in palmitate-treated CCTα-null macrophages compared to controls (Figure 4a). Reduced inflammation in BMDMs was accompanied by a lower ER stress response to palmitate, as indicated by lower induction of ER stress marker gene expression and reduced stress-responsive kinase activation in CCTα-null BMDMs compared to controls (Figure 4b-d).

Furthermore, CCTα-null BMDMs were less susceptible to palmitate-induced cell death than controls (Figure 4-figure supplement 1a). While *Pcyt1a* deficiency was protective against cytotoxicity in response to palmitate, it was detrimental in response to other ER stressors, including thapsigargin (Figure 4-figure supplement 1b) and free cholesterol (Zhang et al., 2000). Finally, cultured peritoneal macrophages isolated from CCTα mKO animals also showed reduced ER stress response to palmitate compared to controls (Figure 4-figure supplement 2). Overall, CCTα-null macrophages were protected against palmitate-induced ER stress and subsequent cytotoxicity and inflammation.

Figure 4 with 2 supplements

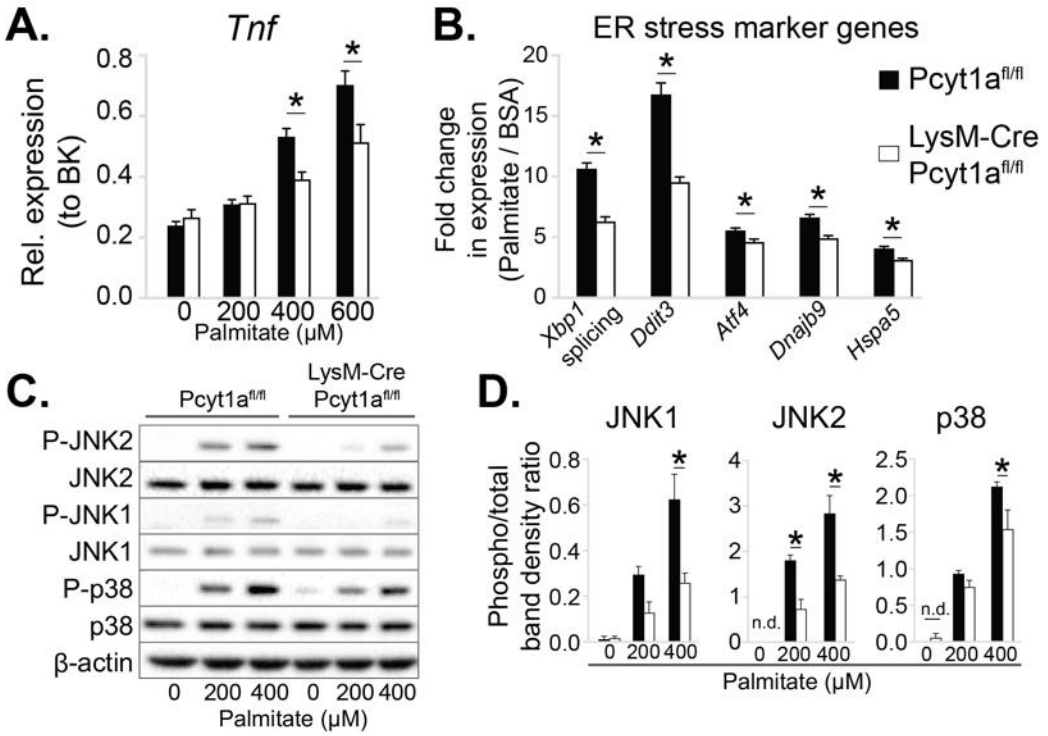

***Pcyt1a* deficiency protects macrophages from palmitate-induced ER stress and inflammation.**
(A) *Tnf* expression levels in Pcyt1a$^{fl/fl}$ (n=5) or Pcyt1a$^{fl/fl}$ LysM-Cre (n=3) BMDMs treated with indicated doses of palmitate for 16 hours.
(B) Fold induction (compared to BSA alone) of indicated ER stress marker gene expression Pcyt1a$^{fl/fl}$ (n=7) or Pcyt1a$^{fl/fl}$ LysM-Cre (n=8) BMDMs treated with 250 μM palmitate for 16 hours.
(C) Representative Western blots and (D) their densitometry quantification of Pcyt1a$^{fl/fl}$ (n=5) or Pcyt1a$^{fl/fl}$ LysM-Cre (n=3) BMDMs treated with indicated doses of palmitate for 16 hours.
∗p < 0.05 between genotypes, error bars indicate SEM. All presented experiments are representative of at least 3 BMDM cultures.

Figure 4-figure supplement 1

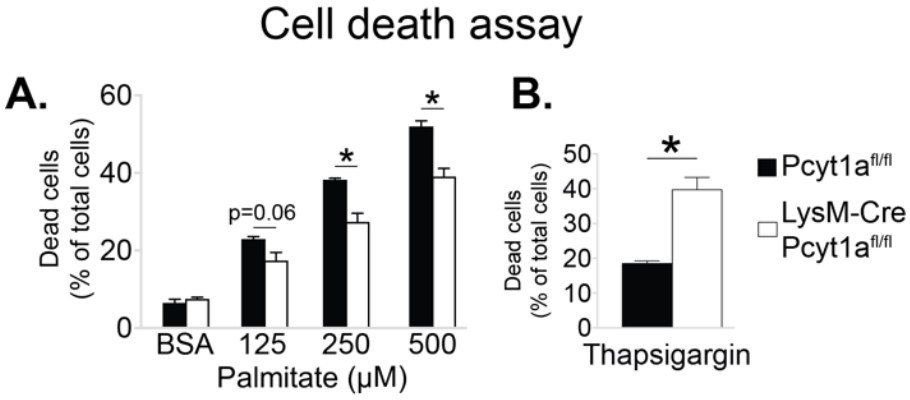

***Pcyt1a* deficiency protects macrophages from palmitate, but not thapsigargin-induced cell death.**
Flow cytometry quantification of dead Pcyt1a$^{fl/fl}$ (n=4) or Pcyt1a$^{fl/fl}$ LysM-Cre (n=4) BMDMs treated with indicated doses of (A) palmitate or (B) 150 nM thapsigargin for 16 hours. ∗p < 0.05 between genotypes, error bars indicate SEM.

Figure 4-figure supplement 2

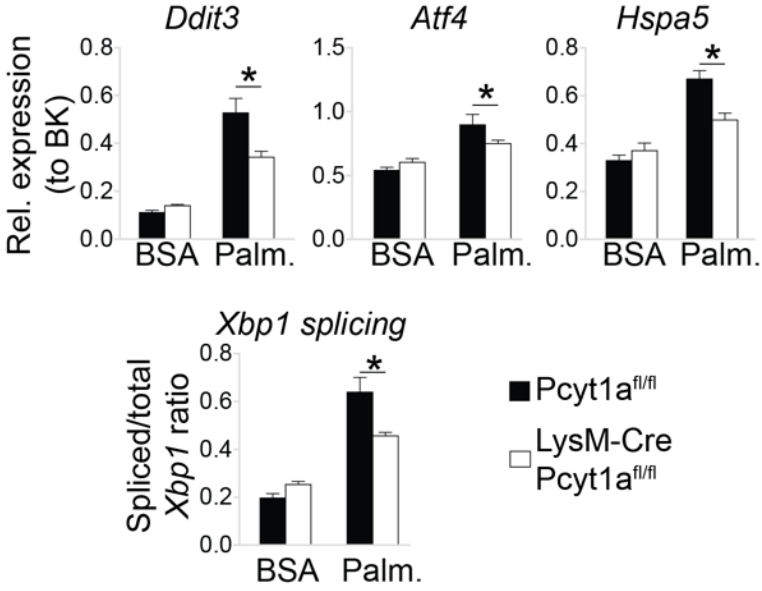

***Pcyt1a* deficiency protects peritoneal macrophages from palmitate-induced ER stress.**
ER stress marker gene expression in cultured peritoneal macrophages from Pcyt1a$^{fl/fl}$ (n=4) or Pcyt1a$^{fl/fl}$ LysM-Cre (n=8) treated with 250 μM palmitate for 16 hours. ∗p < 0.05 between genotypes, error bars indicate SEM.

De novo PC biosynthesis pathway does not incorporate exogenous palmitate into macrophage membrane PCs

We next investigated how mitigating CCTα activity caused a reduction in palmitate-induced ER stress. As the *de novo* PC biosynthesis pathway had been suggested to control the flux of exogenous palmitate into cellular PCs (Robblee et al., 2016), we hypothesised that CCTα-null BMDMs would have a reduced rate of palmitate incorporation into their membranes. In order to test our hypothesis, we traced the incorporation of exogenous palmitate into cellular PCs over time. Surprisingly, CCTα-null and control BMDMs showed no differences in the rate of radiolabelled palmitate appearance in total lipid or PC fractions (Figure 5a-b).

We then attempted to validate our unexpected findings using acute pharmacological inhibition of CCTα by miltefosine. Miltefosine reduced the rate of *de novo* PC synthesis in palmitate-treated BMDMs in a dose-response manner (Figure 5c). In contrast, only 100 μM concentration of miltefosine showed an inhibitory effect on the incorporation of palmitate into membrane PCs (Figure 5c). Importantly, and in line with the evidence from our genetic model, the dose of miltefosine that reduced *de novo* PC biosynthesis rate by 30% (as we have observed in CCTα-null BMDMs, Figure 2-figure supplement 1d) had no effect on the rate of incorporation of exogenous palmitate into cellular PCs in BMDMs (Figure 5c).

It has been proposed that the Kennedy pathway is coupled to endogenous cellular fatty acid synthesis (Ecker et al., 2010; Ridgway and Lagace, 2003). In accordance, acetate incorporation into cellular PCs and total lipids showed a similar fold decrease (approximately 30%) as the reduction in *de novo* PC synthesis rate in CCTα-null

macrophages (Figure 5d-e). Overall, we found that reducing the rate of *de novo* PC synthesis in macrophages proportionally decreased the rate of incorporation of lipids derived from *de novo* lipogenesis, which are known to be incorporated by the Kennedy pathway, but did not affect the rate of exogenous palmitate incorporation into membrane lipids.

Figure 5 with no supplements

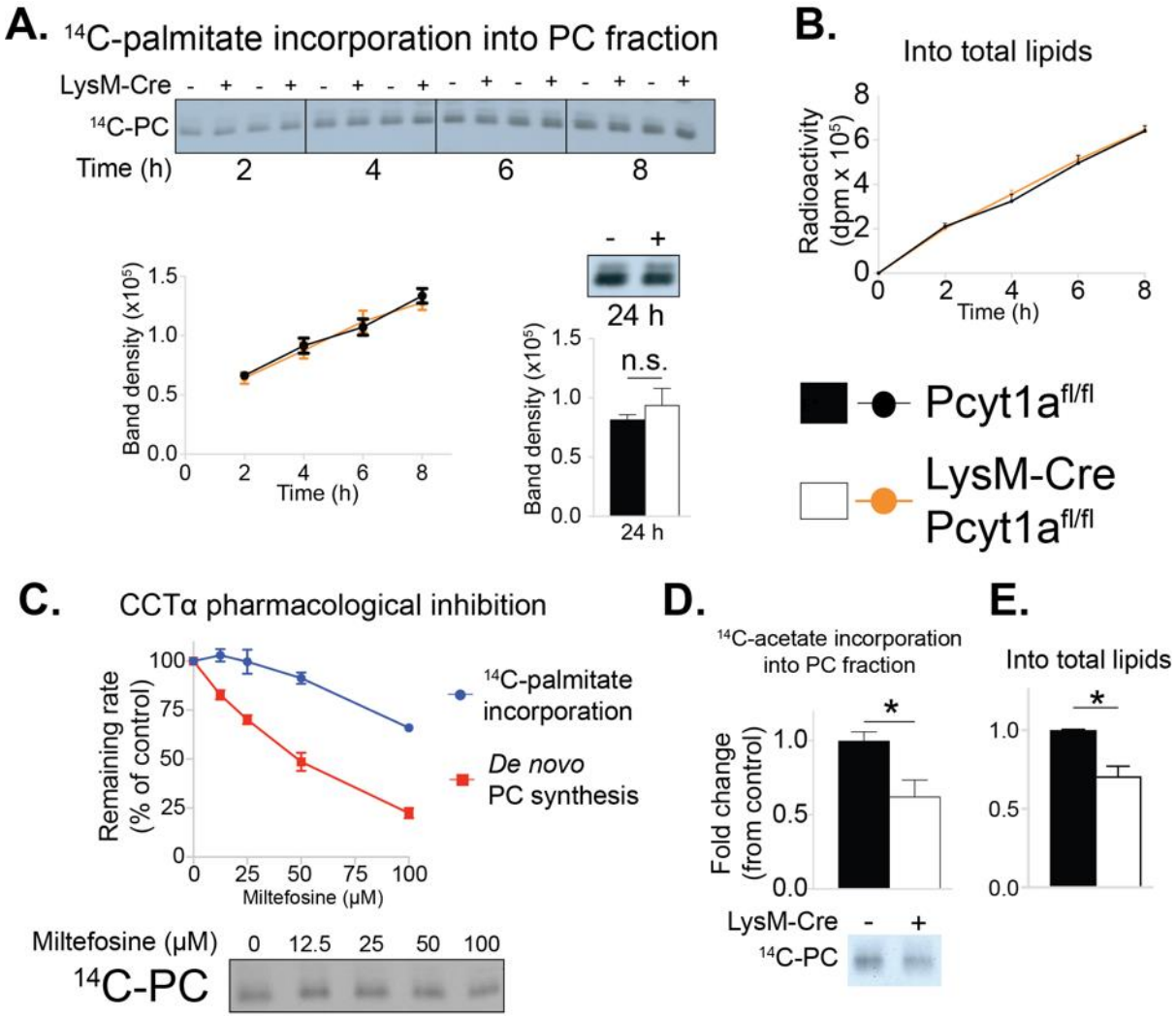

***Pcyt1a* deficiency in macrophages does not affect the rate of exogenous palmitate incorporation into PCs.**

(A) Representative autoradiogram and densitometry quantification of ^{14}C-palmitate incorporation into PCs or (B) total lipids of Pcyt1a$^{fl/fl}$ (n=4) or Pcyt1a$^{fl/fl}$ LysM-Cre (n=4) BMDMs treated with 250 μM palmitate for indicated periods of time.

(C) Inhibition of *de novo* PC biosynthesis (red line) and ^{14}C-palmitate incorporation into PC fraction (blue line) of WT BMDMs (n=4), pretreated with indicated doses of miltefosine for 1 hour and stimulated with 250 μM palmitate for 3 hours. Representative autoradiogram is presented below.

(D) Representative autoradiogram and densitometry quantification of ^{14}C-acetate incorporation into PCs or (E) total lipids of untreated Pcyt1a$^{fl/fl}$ (n=4) or Pcyt1a$^{fl/fl}$ LysM-Cre (n=4) BMDMs over 3 hours, normalised to Pcyt1a$^{fl/fl}$ group average.

∗p < 0.05 between genotypes, error bars indicate SEM. Findings are representative of at least 3 BMDM cultures.

Loss of *Pcyt1a* in macrophages increases membrane PUFA abundance that protects against palmitate-induced ER stress

As our tracer experiments could not explain the diminished ER stress response observed in CCTα-null BMDMs in response to palmitate, we performed global lipidomic analysis of CCTα-null and control BMDMs. As described previously (Tian et al., 2008), total quantities of PC and PE in macrophages were unaffected by *Pcyt1a* deletion (Figure 6-figure supplement 1a). Unexpectedly, CCTα-null macrophages showed an enrichment in PUFA-containing PC levels compared to controls (Figure 6a). Consistent with such observation, the expression of sterol regulatory element-binding protein 1 (SREBP1) target genes, which are known to be downregulated by high levels of PUFA-containing PLs in the ER (Hagen et al., 2010), was lower in CCTα-null macrophages than controls (Figure 6-figure supplement 2). Furthermore, changes in PE composition were similar to qualitative PC changes in CCTα-null and control cells (Figure 6-figure supplement 1b), indicating that reducing *de novo* PC biosynthesis rate promotes PUFA accumulation in membrane PLs.

We observed similar levels of saturated PC species between CCTα-null and control BMDMs under basal conditions (Figure 6b). Interestingly, the increased abundance of PUFA-containing PCs in CCTα-null BMDMs was at the expense of decreased mono- and diunsaturated PC species (Figure 6a-b). We confirmed these findings by analysing total BMDM fatty acid composition, which showed increased relative abundance of arachidonic (20:4n6), docosapentaenoic (22:5n6) and docosahexanoic acids (22:6n3), while palmitoleic and oleic acid levels were reduced in CCTα-null cells compared to controls (Figure 6c).

As expected, palmitate treatment caused a large increase in the abundance of saturated PC species in BMDMs (Figure 6-figure supplement 3b). Interestingly, in palmitate-treated macrophages, PC saturation was increased mostly at the expense of reduced mono- and diunsaturated PCs, while the proportion of 3 or more double bond-containing PC species was largely unaffected by palmitate treatment (Figure 6b and figure supplement 3b). Consequently, CCTα-null BMDMs showed higher membrane PUFA levels than controls even after prolonged treatment with palmitate, leading to diminished palmitate-induced PC saturation (Figures 6b and figure supplement 4). Prolonged palmitate treatment elevated PC:PE ratio to a similar extent in both CCTα-null and control BMDMs, suggesting that changes in total PC levels or PC:PE ratio were unlikely to explain differences in ER stress response between genotypes (Figure 6-figure supplement 3a).

Our lipidomics analysis demonstrated that reduced CCTα activity could affect the levels of fatty acids other than palmitate and specifically resulted in the preferential accumulation of long chain PUFAs. These results were consistent with increased remodelling of PCs, most likely by LPCAT3. Furthermore, our lipid analysis also suggested an explanation for the lower ER stress in response to palmitate. Considerable literature has demonstrated that increased PUFA content in cellular membranes is protective against palmitate induced ER stress (Rong et al., 2013; Yang et al., 2011), suggesting a mechanistic explanation for the protective effects of *Pcyt1a* deletion against palmitate toxicity.

In order to experimentally demonstrate that CCTα-null macrophages exhibited lower ER stress in response to palmitate due to qualitative changes in membrane PL

composition, we performed a rescue experiment of palmitate-treated BMDMs using exogenous arachidonic acid. Compared to palmitate treatment alone, 10:1 molar mixture of palmitate and arachidonate reduced *Tnf* and ER stress marker gene expression to the same basal level in both CCTα-null and control BMDMs (Figure 6d), suggesting that elevated PUFA levels negate the inflammatory effects of palmitate in macrophages lacking *Pcyt1a*. Overall, our results were consistent with a loss of *Pcyt1a* resulting in a shift to a PUFA-rich membrane fatty acid composition that was protective against exogenous palmitate.

Figure 6 with 4 supplements

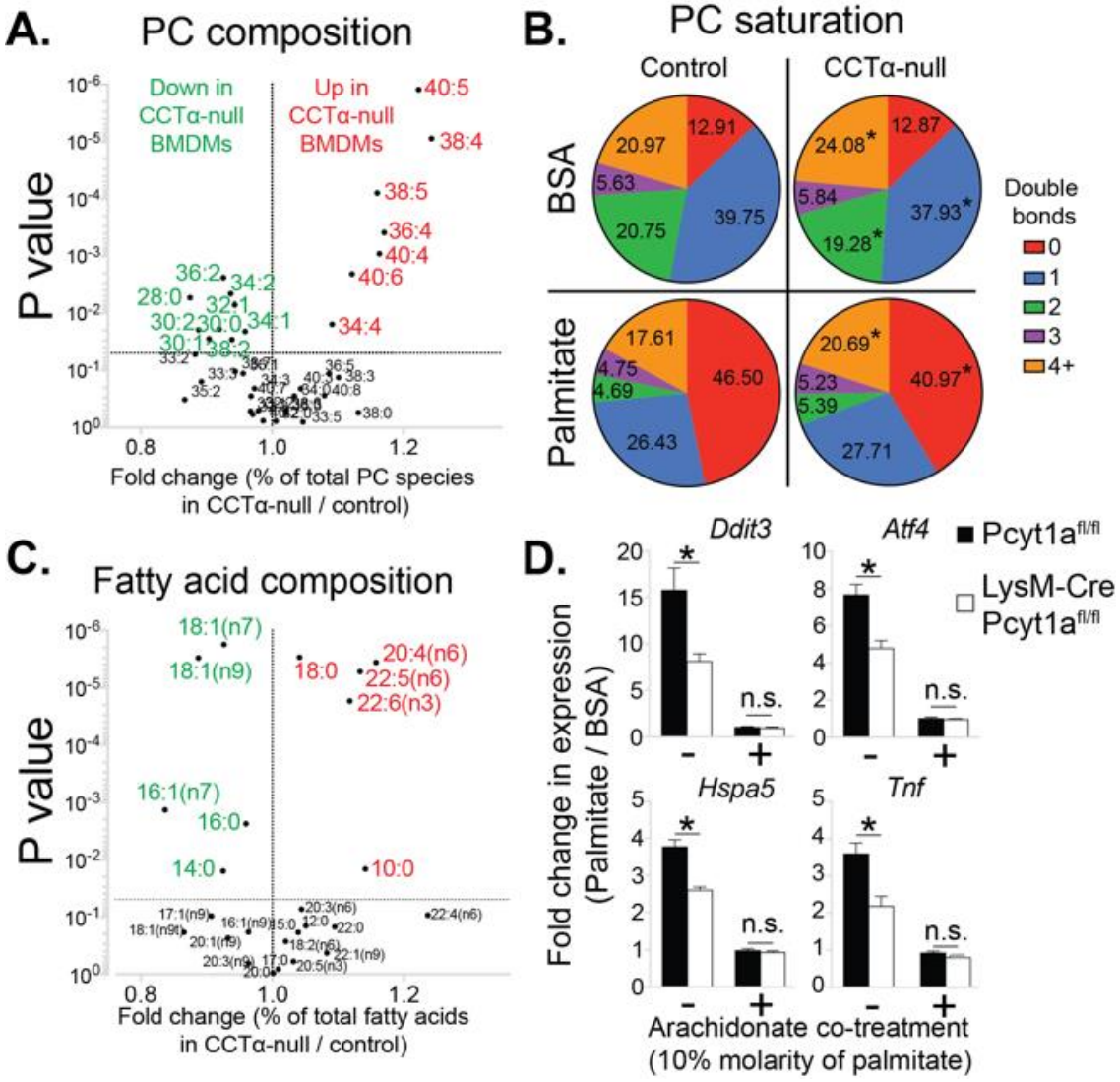

***Pcyt1a* deficiency increases PUFA-containing PC levels in macrophages.**
(A) Volcano plot of indicated PC species, expressed as molar percentage of all measured PCs, in Pcyt1a$^{fl/fl}$ (n=7) or Pcyt1a$^{fl/fl}$ LysM-Cre (n=8) BMDMs.
(B) Pie charts indicating the relative abundance of PC species with different degrees of unsaturation in Pcyt1a$^{fl/fl}$ (n=7) or Pcyt1a$^{fl/fl}$ LysM-Cre (n=8) BMDMs in a basal state or after 16 hour treatment with 250 μM palmitate.
(C) Volcano plot of indicated fatty acid species, expressed as molar percentage of all measured fatty acids, in Pcyt1a$^{fl/fl}$ (n=7) or Pcyt1a$^{fl/fl}$ LysM-Cre (n=8) BMDMs.
(D) Fold induction (compared to BSA alone) of indicated ER stress marker gene and *Tnf* expression in Pcyt1a$^{fl/fl}$ (n=4) or Pcyt1a$^{fl/fl}$ LysM-Cre (n=4) BMDMs after 16-hour treatment with 250 μM palmitate, supplemented with or without 25 μM arachidonate.
∗p < 0.05 between genotypes, error bars indicate SEM.

Figure 6-figure supplement 1

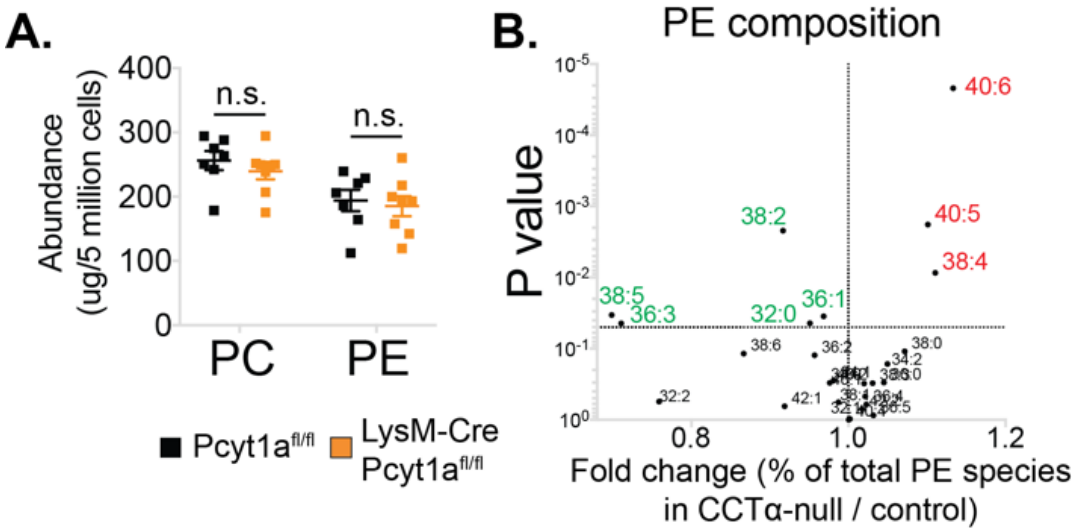

The effects of *Pcyt1a* deficiency on total PC and PE levels and PE composition in macrophages.
(A) Abundance of all detected PC and PE species in Pcyt1a$^{fl/fl}$ (n=7) or Pcyt1a$^{fl/fl}$ LysM-Cre (n=8) BMDMs in a basal state. Error bars indicate SEM.
(B) Volcano plot of indicated PE species, expressed as molar percentage of all measured PEs, in Pcyt1a$^{fl/fl}$ (n=7) or Pcyt1a$^{fl/fl}$ LysM-Cre (n=8) BMDMs in a basal state.

Figure 6-figure supplement 2

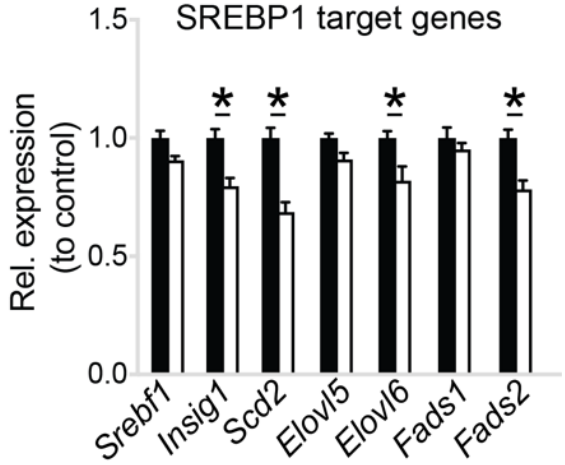

***Pcyt1a* deficiency reduces SREBP1 target gene expression in macrophages.**
Normalised expression of SREBP1 target genes in Pcyt1a$^{fl/fl}$ (n=7, black bars) or Pcyt1a$^{fl/fl}$ LysM-Cre (n=8, white bars) BMDMs in a basal state. ∗p < 0.05 between genotypes, error bars indicate SEM.

Figure 6-figure supplement 3

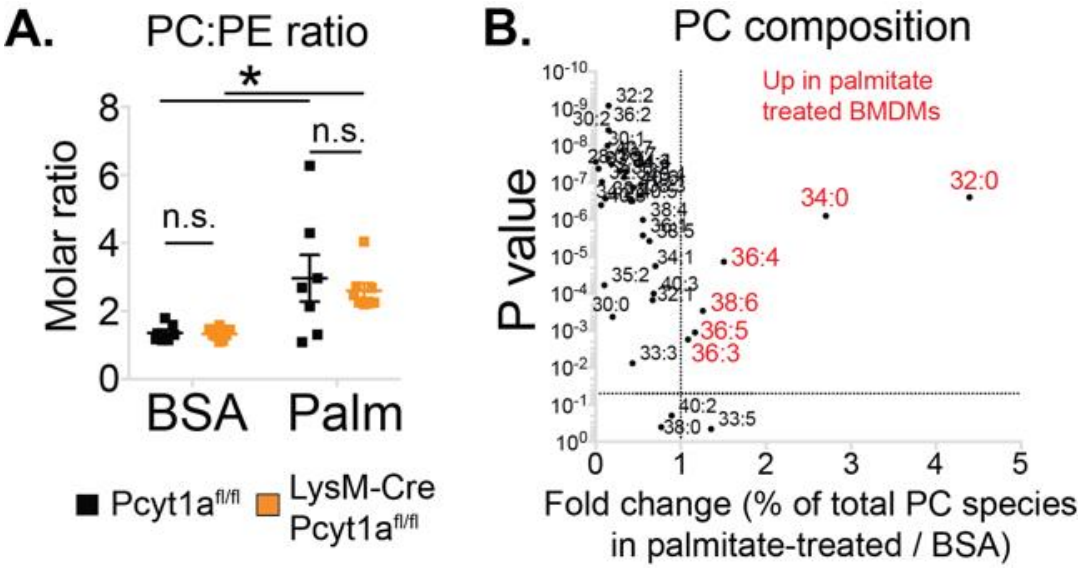

The effects of palmitate treatment on PC to PE ratio and PC composition in macrophages.
(A) PC to PE molar ratio in Pcyt1a$^{fl/fl}$ (n=7) or Pcyt1a$^{fl/fl}$ LysM-Cre (n=8) BMDMs in a basal state or after 16-hour treatment with 250 μM palmitate. ∗p < 0.05 between treatments, error bars indicate SEM.
(B) Volcano plot of indicated PC species, expressed as molar percentage of all measured PCs, in Pcyt1a$^{fl/fl}$ (n=7) BMDMs treated with BSA or 250 μM palmitate for 16 hours.

Figure 6-figure supplement 4

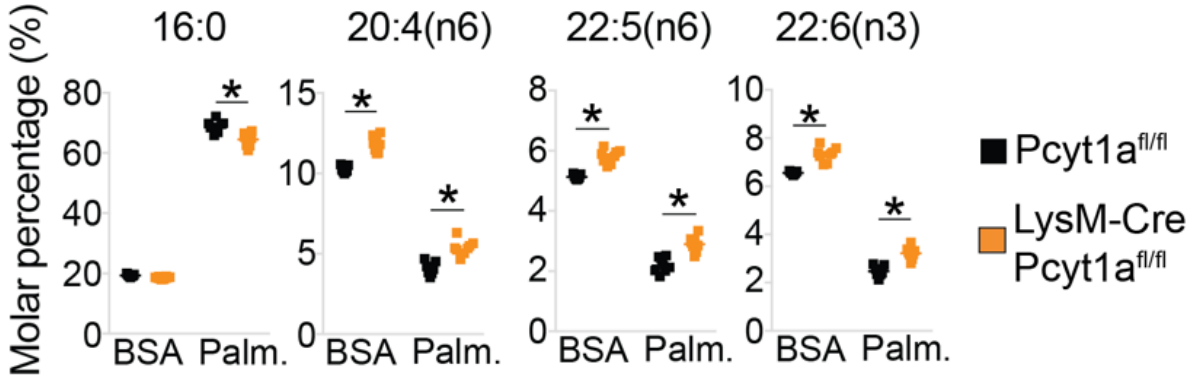

***Pcyt1a* deficiency increases total PUFA levels in macrophages.**
Relative abundance of indicated fatty acids in Pcyt1a$^{fl/fl}$ (n=7) or Pcyt1a$^{fl/fl}$ LysM-Cre (n=8) BMDMs in a basal state or after 16-hour treatment with 250 μM palmitate. ∗p < 0.05 between genotypes, error bars indicate SEM.

Reduced PC turnover promotes membrane PUFA accumulation in *Pcyt1a*-deficient macrophages

Finally, we set out to explain how reduced CCTα activity could lead to an alteration in the fatty acid composition of PC. Our hypothesis was that the increased half-life of membrane PCs in CCTα-null macrophages might allow more time for PCs to be remodelled to contain PUFAs via the Lands cycle. CCTα-null macrophages have previously been shown to have reduced PC turnover rates without changes in total PC levels (Tian et al., 2008) and our experimental findings confirmed these results, as we have observed reduced *de novo* PC synthesis rate and unchanged PC abundance in CCTα-null BMDMs compared to controls (Figure 2-figure supplement 1d and Figure 6-figure supplement 1a).

We next sought to confirm that the increased levels of PUFAs in CCTα-null macrophages were due to a lower turnover of PC. To do so, we performed a pulse-chase experiment using ^{3}H-arachidonic acid. Indeed, CCTα-null BMDMs had increased retention of arachidonic acid in their membranes compared to control cells (Figure 7a). Overall, our results showed that the rate of PC turnover in macrophages is negatively associated with PUFA retention in PLs.

Importantly, while the data from *Pcyt1a*-deficient models demonstrated lower PC turnover, increased levels of long-chain PUFAs and lower PUFA turnover rates, this data came from congenic models lacking *Pcyt1a*. To exclude this being a phenomenon unique to genetically manipulating *Pcyt1a*, we sought to manipulate PC turnover rates via an alternative route. To do so, we pharmacologically blocked PC hydrolysis by inhibiting phospholipase D activity using 1-butanol. In accordance to our hypothesis,

reducing PC turnover by inhibiting PC conversion to phosphatidic acid phenocopied the effects of genetically reduced CCTα activity on cellular membrane fatty acid composition (Figure 7b).

Figure 7 with no supplements

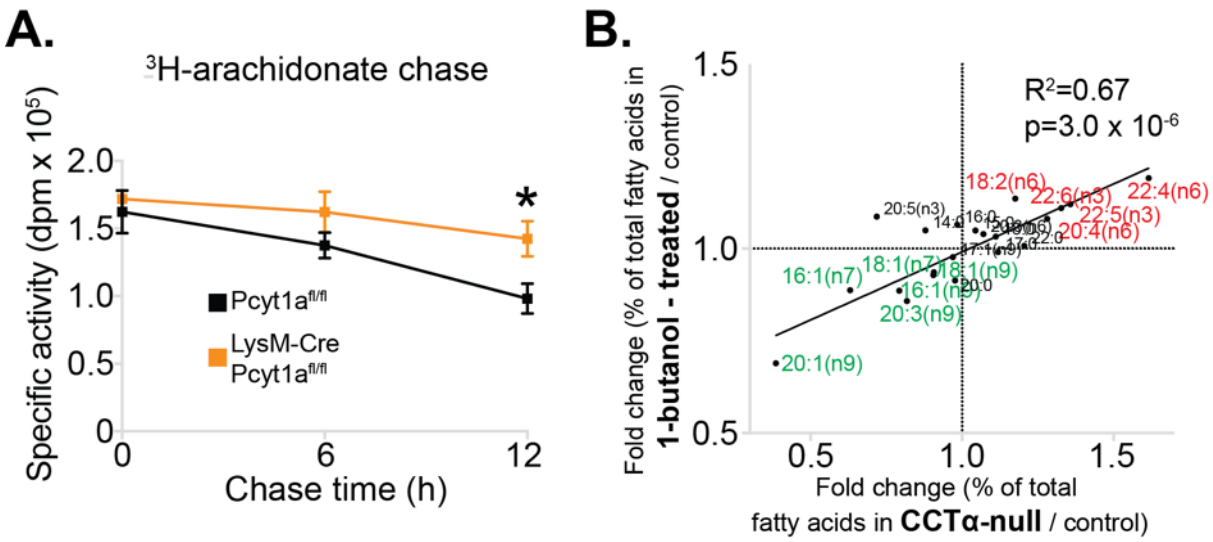

Reduced PC turnover increases membrane PUFA levels in macrophages.
(A) ^{3}H-arachidonate levels in Pcyt1a$^{fl/fl}$ (n=4) or Pcyt1a$^{fl/fl}$ LysM-Cre (n=4) BMDMs, pulsed with tracer amounts of ^{3}H-arachidonate for 16 hours and chased with medium for indicated periods of time. ∗p < 0.05 between genotypes, error bars indicate SEM.
(B) Linear regression analysis of the correlation between fold changes in the molar fatty acid percentage induced by genetic *Pcyt1a* deletion (n=4) and by PLD inhibition using 15 μM 1-butanol for 24 hours (n=4).

Discussion

Here, we demonstrate for the first time that obesity is characterised by an increase in *de novo* PC synthesis pathway in ATMs. We show that the increase in ATM *de novo* PC biosynthesis during obesity is pathophysiologically relevant using a macrophage-specific genetic model of reduced CCTα activity. Reducing *de novo* PC synthesis rate in ATMs alleviates obesity-induced WAT inflammation and improves systemic glucose metabolism. Mechanistically, we show that decreasing CCTα activity in macrophages does not reduce PC levels, but instead leads to a compensatory reduction in PC degradation and maintenance of normal PC levels. Because of this reduced PC turnover, more time is afforded for PC remodelling enzymes to act on PCs, leading to an increase in PUFA-containing PC species that are protective against ER stress in response to palmitate. Our results reveal a novel relationship between the regulation of *de novo* PC synthesis, PC turnover and membrane fluidity.

Our study highlights the importance of CCTα in mediating SFA-induced lipotoxicity in macrophages. Two recent independent reports have suggested that *de novo* PC synthesis is responsible for exogenous palmitate incorporation into membrane PCs (Gianfrancesco et al., 2019; Robblee et al., 2016). Robblee *et al.* based their conclusions on data obtained from pharmacologically inhibiting CCTα using miltefosine at a dose of 100 μM, which inhibits *de novo* PC synthesis rate to a level that also leads to a reduction in exogenous palmitate incorporation, a result we reproduce here (Figure 5C). However, lower doses of miltefosine reduce *de novo* PC synthesis rate without affecting palmitate incorporation into cell membranes. At 25 μM mitefosine, we detect a 30% reduction in *de novo* PC synthesis rate with no reduction in palmitate incorporation, which phenocopies our genetic model of *Pcyt1a* deficiency

in BMDMs. Importantly, our data show that a 30% reduction in *de novo* PC synthesis rate is sufficient to ameliorate ER stress, highlighting the capacity for changes in PC biosynthetic rate to regulate ER stress in a manner that does not require changes in palmitate incorporation. In this publication, we describe such mechanism; that of reduced CCTα activity leading to increased PC half-life and thus permitting the establishment of a membrane composition that is protective against palmitate-induced ER stress. Similarly, Gianfrancesco *et al* have utilised siRNA-mediated *PCYT1A* knockdown in cultured human macrophages to achieve approximately 50% reduction in *de novo* PC synthesis rate and demonstrated that it reduces SFA-induced inflammation. Due to a lack of tracer experiment in their study, we believe that reduced inflammation in their *PCYT1A* knockdown model is due to increased membrane PUFA content, as our experimental findings demonstrate that at 50 μM miltefosine, we detect a 50% reduction in *de novo* PC synthesis rate with no significant reduction in palmitate incorporation.

Further support for a role of PC turnover in regulating ER stress comes from recent work investigating TLR4 signalling. It has recently been shown that palmitate is not a direct TLR4 agonist, but instead requires TLR4 activation-induced changes in intracellular metabolism in order to promote ER stress and inflammation in macrophages (Lancaster et al., 2018). Importantly, it has previously been demonstrated that TLR4 activation increases the rate of *de novo* PC synthesis and PC turnover in macrophages in order to provide a supply of new membranes for secretory vesicle formation in Golgi apparatus (Sanchez-Lopez et al., 2019; Snider et al., 2018; Tian et al., 2008). As such, our findings are in line with a mechanism in which basal TLR4 activation increases sensitivity of cells to palmitate-induced toxicity by

increasing PC turnover. In support of this concept, we demonstrate that decreasing *de novo* PC synthesis protects macrophages from palmitate-driven ER stress and inflammation. Furthermore, two recent reports have demonstrated that TLR4 activation in macrophages increases the transcription of *Slc44a1*, encoding choline transporter CTL1 (Sanchez-Lopez et al., 2019; Snider et al., 2018). As we observed increased *Slc44a1* transcript levels in ob/ob ATMs compared to controls, in future it will be of interest to investigate whether the increase in *Pcyt1a* transcript in ATMs isolated from obese mouse and human WAT is dependent on TLR4 activation.

While ATMs undergo pro-inflammatory activation during obesity, liver macrophages do not (Morgantini et al., 2019). It is likely that for this reason we observed an increased de novo PC synthesis pathway activity in ATMs, but not in liver macrophages isolated from ob/ob mice. While speculative, the absence of pro-inflammatory activation and normal *de novo* PC synthesis rate in liver macrophages could explain why hepatic genes related to metabolism and inflammation were comparable between CCTα-null ob/ob BMT and control mice.

Finally, inactivating mutations in *PCYT1A* gene have been linked to several human pathologies, including retinal dystrophy, spondylometaphyseal dysplasia and lipodystrophy (Hoover-Fong et al., 2014; Payne et al., 2014; Yamamoto et al., 2014). Our results suggest that besides controlling the production of bulk cellular PC mass, CCTα activity can affect the fatty acid composition of cell membranes by regulating their turnover, thus potentially explaining why homozygous *PCYT1A* mutations manifest in specific tissue disorders, and not in a systemic failure of proliferating cells.

Materials and methods

Key resources table

REAGENT or RESOURCE	SOURCE	IDENTIFIER
Antibodies		
anti-CD45	BD Biosciences	564279, RRID:AB_2651134
anti-CD11b	BD Biosciences	564443, RRID:AB_2722548
anti-SiglecF	BD Biosciences	562757, RRID:AB_2687994
anti-F4/80	BioLegend	123116, RRID:AB_893481
Anti-F4/80 (IHC)	Bio-Rad	Cl:A3-1, RRID:AB_1102558
anti-CD206	BioLegend	141723, RRID:AB_2562445
anti-CD11c	BioLegend	117336, RRID:AB_2565268
anti-Ly6G	BioLegend	127608, RRID:AB_1186099
anti-CD301	BioLegend	145704, RRID:AB_2561961
anti-CCTa	Abcam	ab109263, RRID:AB_10859965
anti-beta Actin	Abcam	ab8227, RRID:AB_2305186
anti-P-Thr183/Tyr185 JNK	Cell signalling	9251, RRID:AB_331659
anti-JNK	Cell signalling	9252, RRID:AB_2250373
anti-P-Thr180/Tyr182 p38 MAPK	Cell signalling	4511L, RRID:AB_2139679
anti-p38 MAPK	Cell signalling	9212, RRID:AB_330713
Anti-P-Ser473 AKT	Cell signalling	4060, RRID:AB_2315049
Anti-P-Thr308 AKT	Cell signalling	9275, RRID:AB_329828
Anti-pan AKT	Cell signalling	9272, RRID:AB_329827
Chemicals, Peptides, and Recombinant Proteins		
Insulin	Novo Nordisk	EU/1/02/230/003
STAT 60	AMS Biotech	CS-502
Reverse Transcriptase M-MLV	Promega	M170b
M-MLV RT 5x buffer	Promega	M351A
MgCl2 25mM	Promega	A351B
Random Primers	Promega	C118A
dNTP Mix 10 mM	Promega	U151B
Chlorofom	Sigma	34854
Methanol	Sigma	34860
BF3 Methanol	Sigma	B1127
Hexane	Sigma	34859
Ammonium formate	Sigma	516961
Acetonitrile	VWR	83640.320
1-butanol	Sigma	281549
Miltefosine	Sigma	M5571
Arachidonic acid	Cayman	90010
Palmitic acid	Cayman	1000627
[1-^{14}C]- palmitic acid	Perkin Elmer	NEC075H050UC
[1,2-^{14}C]- acetic acid, sodium salt	Perkin Elmer	NEC553250UC
Methyl-[^{3}H]- choline chloride	Perkin Elmer	NET109250UC
[5,6,8,9,11,12,14,15-^{3}H(N)]- arachidonic acid	Perkin Elmer	NET298Z050UC
Bovine Serum Albumin	Sigma	A8806

Hionic-Fluor scintillation liquid	Perkin Elmer	6013319
Opti-Fluor scintillation liquid	Perkin Elmer	6013199
Ethanol	Sigma	459836
DAKO Real Peroxidase Blocking solution	Agilent	S2023
MOM ImmPress Polymer Reagent	Vector	MP-2400
DAB Peroxidase (HRP) Substrate Kit	Vector	SK-4100
Dako REAL Haematoxylin	Agilent	S2020
Critical Commercial Assays		
Alpha Trak 2 glucose meter	Zoetis	N/A
TruSeq Stranded mRNA Library Prep (96 Samples)	Illumina	20020595
Vybrant Phagocytosis Assay Kit	Thermofisher	V-6694
Deposited Data		
WT and ob/ob adipose tissue macrophage microarray	GEO: GSE36669	Prieur *et al*, 2011
Experimental Models: Organisms/Strains		
Mouse: ob/ob: B6.Cg-Lep_{ob}/J	The Jackson Laboratory	000632
Mouse: LysM-CRE: B6.129P2-$Lyz2_{tm1(cre)Ifo}$/J	Donated by Dr. Susan Jackowski	Clausen *et al*, 1999
Mouse: $Pcyt1a^{fl/fl}$: B6.129-$Pcyt1a_{tm1Irt}$/J	Donated by Dr. Susan Jackowski	Zhang *et al*, 2000
Oligonucleotides		
See Table S3 for the full list of qPCR primer sequences		
Software and Algorithms		
Metabolizer algorithm	http://metabolizer.babelomics.org	Cubuk *et al*, 2018
MassHunter Workstation Software Quantitative Analysis (Version B.07.00)	Agilent Technologies Inc	n/a
Thermo Xcalibur Quan browser integration software (Version 3.0)	Thermofisher	n/a
HALO AI	Indica Labs	n/a
TopHat (Version 2.0.11)		(Kim et al., 2013)
EdgeR		(Robinson et al., 2010)
HiPathia		(Hidalgo et al., 2017)

1

Mice

All animal protocols were conducted in accordance with the UK Home Office and Cambridge University ethical guidelines. Mice were housed 3-4 per cage in a temperature-controlled room (21°C) with a 12 h light/dark cycle, with 'lights on' corresponding to 6 am. Animals had *ad-libitum* access to food and water. A standard chow diet (DS-105, Safe Diets) was administered to all animals from weaning, consisting of 64.3% carbohydrate, 22.4% protein and 13.3% lipid of total calories. Only male mice were used for *in vivo* experiments. Male and female mice (8-20 weeks of age) were used for *in vitro* BMDM cultures.

Generation of myeloid cell-specific CCTα KO mouse

Macrophage-specific *Pcyt1a* knockout mouse (CCTα mKO) was generated by crossing a mouse model containing loxP sequences surrounding *Pcyt1a* alleles ($Pcyt1a^{fl/fl}$) to the LysM-Cre (Clausen et al., 1999) mouse. $Pcyt1a^{fl/fl}$ mouse was generated by Prof. Ira Tabas and Dr. Susan Jackowski as described (Zhang et al., 2000), and was gifted to us on a mixed C57Bl/6J, 129/Sv genetic background by Dr. Suzanne Jackowski. $Pcyt1a^{fl/fl}$ and LysM-Cre lines were backcrossed to a C57Bl6/J genetic background using Marker-Assisted Accelerated Backcrossing (MAX-BAX, Charles River, UK) technology until SNP genotyping confirmed >99% background purity.

All experimental macrophage-specific knockout mice were produced by crossing $LysM^{+/+}$ with $LysM^{+/Cre}$ animals on a floxed/floxed background, yielding a 1:1 Mendelian ratio of control (floxed/floxed $LysM^{+/+}$) to knockout (floxed/floxed $LysM^{+/Cre}$) offspring.

Bone marrow transplant

4-6-week-old WT or ob/ob host mice for bone marrow transplant were purchased from Jackson laboratories and were allowed to acclimatise for at least 2 weeks before the experiment. At 8 weeks of cage, mice were split into two groups of equal average body weight and equal average fed blood glucose concentration (Respective BW and glucose values ±SEM for control and CCTα mKO BMT: 47.1±0.78 g and 46.8+1.68 g, p=0.87; 27.9±3.05mM and 24,4+3.46mM, p=0.45). All mice were given 1% Baytril antibiotic in drinking water a day before irradiation. All mice received two doses of 5.5 Gy of radiation using Caesium 60 source. Two hours post irradiation, donor bone marrow cells (13 million/mouse) were injected into the tail veins of the irradiated mice. The cells from one donor mouse were used for up to 2 host mice. Host mice were then housed at 3-4/cage, with 1-2 mice carrying Pcyt1a$^{fl/fl}$ bone marrow and 1-2 - Pcyt1a$^{fl/fl}$ LysM-Cre bone marrow in each cage. Mice were kept on 1% Baytril for 1 month, monitored and weighed regularly until 12 weeks of age. A single ob/ob mouse carrying Pcyt1a$^{fl/fl}$ bone marrow had to be culled due to health reasons. Mice were then housed under standard housing conditions throughout the duration of the study.

Cells

Culture and differentiation of bone-marrow derived macrophages

Femur and tibia bones from mice were isolated and cleaned, and 10 ml of Roswell Park Memorial Institute Medium (RPMI)-1640 (Sigma) was flushed through each bone using a syringe. Bone marrow cells were counted manually, pelleted by centrifugation, and re suspended in RPMI-1640 with 20-30% L929 conditioned medium, 10% heat-inactivated FBS (Gibco, Thermofisher Scientific) and 100 U/ml penicillin- streptomycin

(Thermofisher Scientific) (macrophage differentiation medium). To differentiate into macrophages, cells were seeded in 10 cm non-culture treated plates (Falcon) at a density of 5x106 cells per plate per 10 ml of macrophage differentiation medium and cultured for 7 days at 37 °C in 5% CO_2. On day 5 of differentiation, medium was removed, and 10 ml of fresh macrophage differentiation medium was added to each plate. On day 7 of differentiation, macrophages were detached using ice-cold PBS containing 1 mM EDTA, counted using Countess automated cell counter (Thermofisher), centrifuged at 500 g, room temperature for 5 min and re suspended in macrophage differentiation medium at the concentration of $5x10^5$ cells/ml. Immediately after, cells were plated for experiments at the following densities: 500 µl/well of 24-well plate, 1 ml/well of 12-well plate, 2 ml/well of 6-well plate and 10 ml per 10 cm plate. Cells were incubated for at least 24 h after plating before conducting experiments.

To make L929 conditioned medium, L929 cells (CCL-1, ATCC) were seeded in DMEM supplemented with 10% heat-inactivated FBS, 100 U/ml penicillin-streptomycin and 2 mM L-glutamine (Sigma) at a density of 500,000 cells per 50 ml of medium per T175 tissue culture flask. Medium was harvested after 1 week of culture, and then 50 mL of fresh DMEM supplemented with 10% heat-inactivated FBS, 100 U/ml penicillin-streptomycin and 2 mM L-glutamine was added onto cells and harvested 1 week later. Batches obtained after the first and second weeks of culture were mixed at a 1:1 ratio, aliquoted and stored at -20 °C.

Isolation and culture of peritoneal macrophages

Immediately after sacrifice, 5 ml of PBS containing 3% FBS was injected into palpitate peritoneal cavity. As much liquid as possible was recovered, and the procedure was repeated two more times with fresh PBS containing 3% FBS. Pooled lavages were centrifuged at 400 g, 4 °C for 5 min. Cells were resuspended in 1 ml DMEM supplemented with 10% heat-inactivated FBS, 100 U/ml penicillin-streptomycin and 2 mM L-glutamine (Sigma) and counted manually. The concentration was adjusted to $5x10^5$ cells/ml, and cells were plated in 24-well plates with 500 µl of cell suspension/well. Medium was changed after 6 hours, and cell stimulations were performed the following day.

Isolation of liver macrophages

Liver macrophages were isolated according to a previously published detailed method (Aparicio-Vergara et al., 2017). Briefly, livers of anesthetized mice were first perfused with calcium-free Hanks` balanced salt solution (HBSS), followed by collagenase digestion. After digestion, the hepatocytes were released by mechanical dissociation of the lobes and underwent several steps of filtration with calcium-containing HBSS and centrifugation at 50g for 3 min. The supernatant containing non-parenchymal cells was loaded on a Percoll gradient (25% and 50%) and centrifuged for 30 min, at 2300 rpm, at 4°C. The interphase ring with enriched liver macrophages was collected. The cells were then plated for 30 min and washed twice before RNA was extracted for subsequent analyses.

Human adipose tissue biopsies

Subcutaneous adipose tissue biopsies were collected from 19 individuals undergoing bariatric bypass surgery, and adipose tissue macrophages were isolated. The

metabolic parameters of individuals have been published earlier (de Weijer et al., 2013). The isolation of macrophages from these adipose tissue biopsies has been described and presented earlier (Virtue et al., 2015).

Methods

Glucose tolerance tests

Mice were fasted for 16 h from 4 pm to 8 am. Mice were single-housed at least 1 h prior to being injected intraperitoneally with 1 mg/kg glucose. Blood samples for glucose measurement were taken at indicated times after the injection.

Insulin tolerance tests

Mice were fasted for 6 h from 8 am to 2 pm. Mice we single-housed at least 1 h prior to being injected intraperitoneally with 0.75 IU/kg of human insulin. Insulin dose of 2.5 IU/kg was used for ob/ob mice. Blood samples for glucose measurement were taken at indicated times after the injection.

Isolation of stromal-vascular fraction (SVF) from WAT

Adipose tissues were removed after sacrifice, chopped thoroughly and resuspended in 10 ml digestion solution containing 7 ml Hanks' Balanced Salt Solution (HBSS, H9269, Sigma), 0.23 g bovine serum albumin (BSA, A8806, Sigma), and 20 mg collagenase type II (C6885, Sigma), filtered through 0.22 µm membrane. The digestion was performed at 37°C for 20 min, with horizontal shaking at 100 rpm. The digestion mixture was then passed through a 100 µm cell strainer (352360, Falcon) into a fresh tube and incubated at room temperature for 10 min, allowing the adipocyte fraction to layer on the surface. Adipocyte fraction was removed by pipetting. The

remaining solution was centrifuged at 400 g, 4°C for 5 min and pellet was re suspended in 1 ml of pre-cooled (at 4°C) FACS buffer (PBS, 1mM EDTA, 3% heat-inactivated FBS). Total SVF cell number was determined by Countess automated cell counter (Thermofisher).

Flow cytometry

SVF or BMDMs were collected and kept in FACS buffer (PBS, 1mM EDTA, 3% HI-FBS) on ice. Cell were stained with LIVE/DEAD (Invitrogen) and non-specific binding was blocked with 5 µg/ml anti-CD16/32. Cell surfaces were then stained with anti-CD45, anti-CD11b, anti-Siglec-F, anti-F4/80, anti-CD301, anti-CD206, anti-CD11c. Cells were gated within the live single cell population as CD45+/Ly6g-/SiglecF-/CD11b+/F4/80+ for ATMs. For BMDMs, median fluorescence for indicated markers was measured in live single cell population. Data were acquired on LSRFortessa (BD Biosciences) using FACS Diva software and analysed with TreeStar FlowJo (Version vX0.7).

Phagocytosis

Bacterial phagocytosis in BMDMs was measured by incubating cells for 2 hours with *E. coli* (K-12 strain) bacteria, labelled with the fluorescent dye fluorescein, according to manufacturer's protocol (Vybrant™ Phagocytosis Assay Kit, ThermoFisher).

Cytokine secretion

BMDMs were stimulated as indicated in figure legend. Culture supernatants were then collected, frozen on dry ice and stored at -80°C until the analysis. Mouse TNF and IL-

6 concentration in supernatants was determined using MesoScale Discovery V-PLEX assay platform, according to manufacturer's protocol.

Radioisotope labelling

For radiolabelling experiments, radioisotope tracers were dissolved in macrophage differentiation medium at the following concentrations: 0.074 MBq/ml for methyl-[^{3}H] choline chloride (for PC synthesis assays), 0.06 MBq/ml for [1-^{14}C]-palmitic and [^{3}H]-arachidonic acids, and 0.148 MBq/ml for [1-^{14}C] acetic acid. BMDMs were plated at the standard densities in 24-well plates for PC synthesis and fatty acid incorporation/chase assays and in 6-well plates for lipid class analysis by thin-layer chromatography.

Radioactivity in total cells was determined by lysing cells in 100 µl of PBS containing 1% Triton^{TM} X-100, adding the lysate to scintillation vial containing 5 ml of Hionic-Fluor scintillation liquid and subjecting it to liquid scintillation counting (LSC).

Fatty acid treatments

All fatty acid treatments were done using FFAs conjugated to BSA (fatty acid and endotoxin free, A8806, Sigma). The conjugation was performed by preparing a sterile-filtered 5% BSA solution in macrophage differentiation medium. Both 5% BSA medium and concentrated fatty acid solution (100 mM of fatty acid in ethanol) were heated at 60°C before adding fatty acid solution dropwise into 5% BSA medium in order to make a medium containing 2.5 mM fatty acid and 5% BSA (approximately 10:3 fatty acid to BSA molar ratio). This medium was then sonicated until it became completely clear and used as a stock solution for stimulations on the same day without sterile filtering.

FFA-free BSA solution with equivalent amount of ethanol was used as a control. In dose-response experiments, the amount of BSA and ethanol in each condition was adjusted to the highest dose of palmitate. Unless otherwise indicated, fatty acid treatments were performed overnight for 16 hours.

Extraction and quantification of RNA

RNA from cells was extracted using RNeasy Plus Mini kit (74106, Qiagen) following manufacturers' instructions. 30 µl of RNAse-free water was used for elution.

RNA from tissues was harvested by adding 1 ml of RNA Stat-60 reagent (Tel Test) to approximately 100 mg of frozen tissue placed in a Lysing Matrix D tube (MP Biomedicals). Samples were homogenised using a FastPrep homogeniser (MP Biomedicals) for 2 x 45 s at 5.5 m/s and centrifuged at 14,000 g for 5 min to pellet debris. The aqueous phase was transferred to a fresh tube containing 200 µl chloroform. Samples were mixed and centrifuged at 14,000 g, 4°C for 15 min. The clear upper phase containing RNA was removed and precipitated by mixing it with 500 µl isopropanol and incubating at room temperature for 10 min. Samples were centrifuged at 14,000 g, 4°C for 10 min and supernatants were discarded. RNA pellets were then washed with 70% ethanol, air-dried and re-suspended in 100 µl of RNAse-free water.

RNA concentration and purity were determined using Nanodrop ND-1000 spectrophotometer (Thermofisher Scientific). The absorbance was measured at 260 nm against RNAse-free water. A single A260 unit was assumed to be equal to 40 µg/mL of RNA. All RNA samples were stored at -80°C for subsequent processing.

Quantitative real-time polymerase chain reaction (qRT-PCR)

Complementary DNA (cDNA) was generated using Promega reagents in a 20 µl reaction as follows: 500 ng RNA was added to 1 x M-MLV reverse transcriptase master mix (M351A) with 2.5 mM MgCl2 (A351B), 1.25 mM dNTPs (U151B), and 5 µg/mL random hexamers (C118A), and denatured at 65°C for 5 min before being transferred directly to ice in order to prevent the reassembly of the secondary structures of RNA. After the addition of 1 µL of M-MLV reverse transcriptase (M170b), the reaction was incubated at 37°C for 1 h for cDNA synthesis and 95°C for 5 min for enzyme denaturation. cDNA was diluted 75-fold in RNAse-free water and stored at -20°C.

qRT-PCR was performed in a 13 µL reaction with 5 µl of diluted cDNA, 6.5 µl of 2x TaqMan or SYBR Green reagent (Applied Biosystems), 1.3 µl of 3 mM forward and reverse primer mix (including 1.5 mM of probe for TaqMan reactions) and 0.2 µl of RNAse-free water according to the default manufacturer's protocol (Applied Biosystems). Primer sequences are described in Table S2. Reactions were run in duplicate for each sample and quantified using the ABI Prism 7900 sequence detection system (Applied Biosystems). Duplicates were checked for reproducibility, and then averaged; 'no reverse transcriptase' controls were included to check for genomic DNA contamination, and 'no template' controls were included to check for the formation of primer dimers. Product specificity was determined using a dissociation curve for SYBR green reactions. A standard curve generated from a pool of all cDNA samples was used for quantification. The expression of genes of interest was normalized using BestKeeper method to the geometric average of 3-4 housekeeping

genes (for mouse: *18s, 36b4* and *Tbp*; for human: *Actb, B2m, Gapdh* and *Polr2a*), and data was expressed as arbitrary units or normalised to the average of control group.

Whole white adipose tissue RNA sequencing and analysis

2 μg of eWAT RNA was used to generate barcoded sequencing libraries using TruSeq® Stranded mRNA Library Preparation Kit (Illumina) following manufacturer's instructions. After adjusting for concentration, the sequencing libraries were combined into 96-plex pools. The pooled libraries were sequenced on 3 lanes of an Illumina HiSeq 4000 instrument at single-end 50bp (SE50), yielding an average of 15.7 million reads per sample. Library preparation was performed by the Genomics and Transcriptomic Core at the Institute of Metabolic Science. The sequencing was performed at the Genomics Core, Cancer Research UK Cambridge Institute.

RNA sequencing data was aligned using TopHat (V2.0.11) to the mouse GRCm38 genome and genes were counted using HTseq-count (V0.8.0) by the Genomics and Transcriptomic Core at the Institute of Metabolic Science. Data normalisation and differential gene expression analysis was performed with edgeR using TMM and generalized linear model methods, respectively. Pathway activity analysis was performed using HiPathia algorithm.

Extraction of RNA, RNA sequencing and analysis of liver macrophages

RNA extraction was performed using the TRIzol Reagent according to the manufacturer's instructions (15596018, ThermoFisher).

RNA libraries were prepared using TruSeq® Stranded mRNA kit (Illumina). The concentration of indexed libraries was quantified by RT–qPCR using the Universal Kapa Library Quantification Kit (KAPA Biosystems). Final libraries were normalized and sequenced on an Illumina HiSeq 2000 sequencer.

Raw fastq-files were aligned against the murine genome version mm10 using TopHat (v2.0.13) with all default options. BAM files containing the alignment results were sorted according to the mapping position. mRNA quantification was performed using FeatureCounts from the Subread package against the GRCm38-gencode transcripts database version seven (gencode.vM7.annotation.gtf) and the GRCh38-genocode transcripts database version 24 (gencode.v24.annotation.gtf) to obtain read counts for each individual Ensembl gene. The read count table of the dataset was normalized separately using DESeq2.

Protein extraction and quantification

BMDMs were treated as described in legend, washed once with ice-cold PBS and lysed in ice-cold RIPA buffer (50 mM Tris-HCl, 150 mM NaCl, 1 mM EDTA, 0.1% SDS, 0.5% sodium deoxycholate, 1% NP-40, pH 7.4) containing Pierce™ protease and phosphatase inhibitors (88668, Thermofisher Scientific). 150 µl of RIPA buffer was used to lyse 10^6 cells. Frozen white adipose tissue samples (approximately 50 mg) were ground in liquid nitrogen using mortar and pestle, and powdered tissue was then dissolved in 200 µl ice-cold RIPA buffer. Lysates were collected and centrifuged at 14,000 g, 4°C for 10 min to remove cell debris.

Protein concentration was determined by DC Protein assay (5000111, Biorad) according to manufacturer's instructions.

Western blotting

Protein lysates were diluted in NuPAGE™ LDS sample buffer (NP0007, Thermofisher Scientific) containing 2.5% 2-mercaptoethanol and boiled at 95°C for 5 min. 10 µg of protein was then separated by electrophoresis using NuPAGE™ SDS-polyacrylamide gels (Thermofisher Scientific) and transferred to nitrocellulose membranes using the iBlot® Dry Blotting System (Thermofisher Scientific). Membranes were blocked for 1 h in 5% fat-free milk (Marvel) or 5% BSA in Tris-buffered saline containing 0.05% Tween (TBST) at room temperature and incubated overnight at 4°C with the appropriate primary antibody. Bound primary antibodies were detected using peroxidase-coupled secondary anti-rabbit antibody (7074, Cell signalling) and enhanced chemiluminescence (WBLUF0500, Millipore). Blots were exposed digitally using the ChemiDoc MP System (Bio-Rad), and bands were quantified using Image Lab™ software (Bio-Rad). The expression of proteins was normalised to a housekeeping protein (β-actin), and the phosphorylation status was determined by normalising to a respective total protein. All protein quantification data is expressed as arbitrary units.

Adipose tissue histology and imaging

Adipose tissue samples for histology were placed in 10% formalin overnight, then transferred to 70% ethanol before embedding in paraffin. Different 4 µm sections were obtained from FFPE blocks and extra-coated with paraffin to preserve tissue integrity.

After incubating overnight at 37°C, sections were dewaxed using xylene and 100% industrial methylated spirits, then washed under running water for 5 min and kept in TBST. The sections were stained as follows: 1) blocking endogenous peroxidases for 5 min (DAKO Real Peroxidase Blocking solution, S2023); 2) wash in TBST; 3) blocking using serum for 20 min; 4) primary anti-F4/80 antibody incubation for 60 min; 5) wash in TBST for 5 min; 6) 30 min incubation with MOM ImmPress Polymer Reagent (MP-2400); 7) wash in TBST; 8) DAB solution (5-10 minutes) prepared according to the manufacturer's instruction (DAB Peroxidase substrate kit, SK-4100); 9) wash in TBST; 10) 1 min incubation with Dako REAL Haematoxylin (S2020). The sections where then washed in tap water, dehydrated in graded alcohols, cleared in xylene and mounted.

All eWAT slides were scanned using a Zeiss Axio Scan Z1 and analysed using HALO software (Indica Labs, Corrales, NM). The 'tissue classifier module', utilising a state-of-the-art machine learning algorithm to identify tissue types based on colour, texture, and contextual features, was used to distinguish areas containing F4/80-positive cells (marked in dark green). 'Vacuole Quantification module' was then applied to analyse the adipocytes in dark green areas and in a whole section. Intact vacuoles completely surrounded by F4/80-positive cells were considered as CLS, while whole section vacuole analysis was used to determine average adipocyte area. The analyses were performed on the whole section to avoid selection bias; tissue edges were excluded using manual annotation. Halo was "trained-by-example" on randomly selected images, and then the analysis was extended on the whole batch of sections with HALO automated pipeline.

Lipid extraction

Total lipids from cells were extracted using a modified Folch extraction method. Glass pipettes were used throughout the procedure in order to avoid plastic-bound lipid contamination. 1 ml of HPCL-grade chloroform: methanol 2:1 v/v mixture was added to cell samples in a glass vial. Where applicable, appropriate amounts (calculated by approximating the average abundance of every fatty acid within the sample and adding matching amounts of standard) of 1,2-diundecanoyl-sn-glycero-3-phosphocholine (phospholipid standard, 850330C, Sigma) were included in extraction mixture as internal standard. Samples were homogenised by vortexing for 15 s. 200 µl of HPLC-grade water was added to each sample before vortexing for 2 min and centrifuging at 4000 g for 10 min. 700 µl of the lower lipid fraction was transferred to a 7 ml glass tube. A second extraction was performed by adding 700 µl of fresh HPLC-grade chloroform followed by vortexing and centrifugation as above. 900 µl of lower lipid fraction was collected and pooled with the first 700µl fraction (total 1600 µl). Collected lipid fractions were dried under nitrogen stream. Dried lipids were stored at -20°C for subsequent processing, or resuspended in 100 µl chloroform, transferred to scintillation vials containing 5 ml of Opti-Fluor scintillation liquid (6013199, Perkin Elmer) and subjected to LSC.

Thin-layer chromatography

BMDMs were treated in 6-well plates as indicated in legend and lipids were labelled as described. Lipids from cells were extracted and solubilised in 50 µl of HPLC-grade chloroform. 20 µl of lipids were then spotted at the bottom of 20 cm x 20 cm thin layer chromatography (TLC) silica plates (Z292974, Sigma). TLC plates were placed into hermetic glass chambers containing 250 ml of 65:25:4 chloroform: methanol:

ammonium hydroxide v/v solution for phospholipid separation. Plates were allowed to develop until the solvent front was approximately 2 cm below the top of the plate. Plates were dried under laminar flow and incubated with radiographic films (47410, Fujifilm) in the dark for 1-3 days at room temperature. Radiographic films were developed using automated film developer and scanned. ImageJ software (NIH) was used to calculate the density of the bands on scanned radiograms.

LC-MS lipid analysis

To the previously dried lipid samples, 60 µL of the lipid internal standard was added (methanol containing CE(18:0)$_{d6}$, Ceramide(16:0)$_{d31}$, FA(15:0)$_{d29}$, LPC(14:0)$_{d42}$, PA(34:1)$_{d31}$, PC(34:1)$_{d31}$, PE(34:1)$_{d31}$, PG(34:1)$_{d31}$, PI(34:1)$_{d31}$, PS(16:0)$_{d62}$, SM(16:0)$_{d31}$, TG(45:0)$_{d29}$, and TG(54:0)$_{d35}$, all at 10 µg/mL). The samples were then thoroughly vortexed, then dried under a gently stream of nitrogen. The samples were then reconstituted by adding 740 µL of 4:1 mix of isopropanol and acetonitrile, respectively, and vortexed ensuring there was no undissolved material. The samples were then analysed by LC-MS analysis.

Chromatographic separation was achieved using Acquity UPLC CSH C18 (50 mm x 2.1 mm, 1.7 µm) LC column with a Shimadzu UPLC system (Shimadzu UK Limited, Wolverton, Milton Keynes). The column was maintained at 55 ^{o}C with a flow rate of 0.5 mL/min. A binary mobile phase system was used with mobile phase A; 60:40 acetonitrile to water, respectively, with 10 mM ammonium formate, and mobile phase B; 90:10 isopropanol to acetonitrile, respectively, with 10 mM ammonium formate. The gradient profile was as follows; at 0 minutes_40% mobile phase B, at 0.4 minutes_43% mobile phase B, at 0.45 minutes_50% mobile phase B, at 2.4 minutes_54% mobile

phase B, at 2.45 minutes_70% mobile phase B, at 7 minutes_99% mobile phase B, at 8 minutes_99% mobile phase B, at 8.3 minutes_40% mobile phase B, at 10 minutes_40% mobile phase B.

Mass spectrometry detection was performed on an Exactive Orbitrap mass spectrometer (Thermo Scientific, Hemel Hempstead, UK) operating in positive/negative ion switching mode. Heated electrospray source was used, the sheath gas was set to 40 (arbitrary units), the aux gas set to 15 (arbitrary units) and the capillary temperature set to 300 °C. The instrument was operated in full scan mode from m/z 150–1200 Da.

Data processing was completed using Thermo Xcalibur Quan browser integration software (Thermo Scientific, Hemel Hempstead, UK). The identification of the lipid species was determined by an MS-signal for the corresponding theoretically calculated m/z accurate mass found at the expected retention time. The semi-quantitation of the lipids was calculated by the integration of the analyte MS-signal relative to the lipid class internal standard concentration.

Quantitative analysis of fatty acid methyl esters (FAMEs)

In order to derive FFAs and esterified fatty acids from complex lipids into FAMEs, 750 µl of HPLC-grade chloroform: methanol 1:1 v/v solution was added to previously dried lipids in 7 ml glass vials. 125 µl of 10% boron trifluoride in methanol (134821, Sigma) was then added into each vial. Vials were sealed and incubated in an oven at 80°C for 90 min in order to hydrolyse fatty acid-glycerol and fatty acid-cholesterol ester bonds and form FAMEs. Samples were allowed to cool, and 1 ml of HPLC-grade n-

Hexane and 500 µl of HPLC-grade water were added. Samples were briefly vortexed and centrifuged at 2000 g using benchtop centrifuge. The upper organic layer was transferred into 2 ml gas chromatography glass vials and dried under nitrogen stream.

Gas chromatography-mass spectrometry was performed with Agilent 7890B gas chromatography system linked to Agilent 5977A mass spectrometer, using AS3000 auto sampler. A TR-FAME column (length: 30 m, inter diameter: 0.25 mm, film size: 0.25 µm, 260M142P, Thermofisher Scientific) was used with helium as carrier gas. Inlet temperature was set at 230°C. Dried FAME samples were re-suspended in 100 µl HPLC-grade n-Hexane. 1 µl of this solution was injected for analysis. The oven programme used for separation was as follows: 100°C hold for 2 min, ramp at 25°C/min to 150°C, ramp at 2.5°C/min to 162°C and hold for 3.8 min, ramp at 4.5°C/min to 173°C and hold for 5 min, ramp at 5°C/min to 210°C, ramp at 40°C/min to 230°C and hold for 0.5 min. Carrier gas flow was set to constant 1.5 ml/min. If the height of any FAME peaks exceeded 10^8 units, sample was re-injected with 10:1 – 100:1 split ratio. Identification of FAME peaks was based on retention time and made by comparison with those in external standards (Food industry FAME mix, 35077, Restek).

Peak integration and quantification was performed using MassHunter Workstation Quantitative Analysis software (version B.07.00, Agilent). Specific high-abundance ions from total ion chromatogram were chosen to calculate each fatty acid peak. The values for each fatty acid were expressed in molar percentages by dividing the area of each peak by the sum of all peak areas for a given sample. This analysis accounted for differences in total lipid content between samples.

Statistical analysis and graphical representation of data

All data from experiments is represented as a mean, with error bars showing standard error of the mean and the number of replicates stated in legend. Some data is represented as a fold-change, and it is stated in legend to what value the data represented was normalised to generate the fold-change. A student's t-test was used to compare two groups; one-way analysis of variance (ANOVA) was used to compare more than 2 groups, followed by Bonferonni's post-hoc test. Where more than one factor influenced the variable being measured, 2-way ANOVA was used to test for a significant effect of each factor as well as an interaction between factors.

All statistical tests were performed and graphs were generated using GraphPad Prism 6 software. Graphs and figures were edited for presentation using Adobe Illustrator CC 2015 software.

Metabolizer algorhythm used to analyse microarray data can be accessed at http://metabolizer.babelomics.org and its methodology is presented in recent publications (Cubuk et al., 2018b; 2018a).

Acknowledgements

Pcyt1a$^{fl/fl}$ and LysM-Cre mice were a kind gift from Dr. Susan Jackowski. We thank Daniel Hart, Sarah Grocott, Charley Beresford, Jade Bacon, Laura McKinven, Eerika Rasijeff and Agnes Lukasik for their excellent technical assistance in the animal work. All animal work was carried out in the Disease Model Core (MRC Metabolic Diseases Unit [MRC_MC_UU_12012/5]; Wellcome Trust Strategic Award [100574/Z/12/Z]). We also thank Brian Lam and Marcella Ma from the Genomics and Transcriptomics Core, James Warner from the Histology core and Gregory Strachan from the Imaging core for their technical assistance. All serum biochemistry and cytokine secretion analysis were conducted by the Biochemistry Assay Lab (MRC Metabolic Diseases Unit [MRC_MC_UU_12012/5]). We thank the Wellcome Trust [102354/Z/13/Z], BHF [RG/18/7/33636], MRC [MC_UU_12012/2], Spanish Ministry of Economy and Competitiveness [SAF2017-88908-R], AstraZeneca through the ICMC (M.A.), the Swedish Research council (M.A.: 2015-03582) and the Strategic Research Program in Diabetes at Karolinska Institutet (M.A.) for funding this work. The research leading to these results has also received support from the Innovative Medicines Initiative Joint Undertaking under EMIF grant agreement n°115372, resources of which are composed of financial contribution from the European Union's Seventh Framework Programme (FP7/2007-2013) and EFPIA companies' in kind contribution.

Author contributions

K.P. and S.V. designed and conducted experiments and wrote the manuscript. G.B. conducted experiments. B.J. and A.K. conducted LC-MS lipid analysis. C.C. and J.D. performed bioinformatics analysis of transcriptomic data. C.M. and M.A. provided transcriptomic data and analysis of liver macrophages. M.S. provided human

adipose tissue samples and isolated ATMs. A.V.-P. supervised the study and wrote the manuscript.

Declaration of interests

The authors declare no competing interests.

References

Aparicio-Vergara, M., Tencerova, M., Morgantini, C., Barreby, E., Aouadi, M., 2017. Isolation of Kupffer Cells and Hepatocytes from a Single Mouse Liver. Methods Mol. Biol. 1639, 161–171. doi:10.1007/978-1-4939-7163-3_16

Ariyama, H., Kono, N., Matsuda, S., Inoue, T., Arai, H., 2010. Decrease in membrane phospholipid unsaturation induces unfolded protein response. J. Biol. Chem. 285, 22027–22035. doi:10.1074/jbc.M110.126870

Clausen, B.E., Burkhardt, C., Reith, W., Renkawitz, R., Förster, I., 1999. Conditional gene targeting in macrophages and granulocytes using LysMcre mice. Transgenic Res. 8, 265–277.

Cubuk, C., Hidalgo, M.R., Amadoz, A., Pujana, M.A., Mateo, F., Herranz, C., Carbonell-Caballero, J., Dopazo, J., 2018a. Gene expression integration into pathway modules reveals a pan-cancer metabolic landscape. Cancer Res. canres.2705.2017. doi:10.1158/0008-5472.CAN-17-2705

Cubuk, C., Hidalgo, M.R., Amadoz, A., Rian, K., Salavert, F., Pujana, M.A., Mateo, F., Herranz, C., Caballero, J.C., Dopazo, J., 2018b. Differential metabolic activity and discovery of therapeutic targets using summarized metabolic pathway models. bioRxiv 367334. doi:10.1101/367334

de Weijer, B.A., Aarts, E., Janssen, I.M.C., Berends, F.J., van de Laar, A., Kaasjager, K., Ackermans, M.T., Fliers, E., Serlie, M.J., 2013. Hepatic and peripheral insulin sensitivity do not improve 2 weeks after bariatric surgery. Obesity 21, 1143–1147. doi:10.1002/oby.20220

Ecker, J., Liebisch, G., Englmaier, M., Grandl, M., Robenek, H., Schmitz, G., 2010. Induction of fatty acid synthesis is a key requirement for phagocytic differentiation of human monocytes. Proc. Natl. Acad. Sci. U.S.A. 107, 7817–7822. doi:10.1073/pnas.0912059107

Fu, S., Yang, L., Li, P., Hofmann, O., Dicker, L., Hide, W., Lin, X., Watkins, S.M., Ivanov, A.R., Hotamisligil, G.S., 2011. Aberrant lipid metabolism disrupts calcium homeostasis causing liver endoplasmic reticulum stress in obesity. Nature 473, 528–531. doi:10.1038/nature09968

Gianfrancesco, M.A., Dehairs, J., L'homme, L., Herinckx, G., Esser, N., Jansen, O., Habraken, Y., Lassence, C., Swinnen, J.V., Rider, M.H., Piette, J., Paquot, N., Legrand-Poels, S., 2019. Saturated fatty acids induce NLRP3 activation in human macrophages through K+ efflux resulting from phospholipid saturation and Na, K-ATPase disruption. Biochim Biophys Acta Mol Cell Biol Lipids. doi:10.1016/j.bbalip.2019.04.001

Hagen, R.M., Rodriguez-Cuenca, S., Vidal-Puig, A., 2010. An allostatic control of membrane lipid composition by SREBP1. FEBS Lett. 584, 2689–2698. doi:10.1016/j.febslet.2010.04.004

Heng, T.S.P., Painter, M.W., Immunological Genome Project Consortium, 2008. The Immunological Genome Project: networks of gene expression in immune cells. Nature Immunology 9, 1091–1094. doi:10.1038/ni1008-1091

Hidalgo, M.R., Cubuk, C., Amadoz, A., Salavert, F., Carbonell-Caballero, J., Dopazo, J., 2017. High throughput estimation of functional cell activities reveals disease

mechanisms and predicts relevant clinical outcomes. Oncotarget 8, 5160–5178. doi:10.18632/oncotarget.14107

Holzer, R.G., Park, E.-J., Li, N., Tran, H., Chen, M., Choi, C., Solinas, G., Karin, M., 2011. Saturated fatty acids induce c-Src clustering within membrane subdomains, leading to JNK activation. Cell 147, 173–184. doi:10.1016/j.cell.2011.08.034

Hoover-Fong, J., Sobreira, N., Jurgens, J., Modaff, P., Blout, C., Moser, A., Kim, O.-H., Cho, T.-J., Cho, S.Y., Kim, S.J., Jin, D.-K., Kitoh, H., Park, W.-Y., Ling, H., Hetrick, K.N., Doheny, K.F., Valle, D., Pauli, R.M., 2014. Mutations in PCYT1A, encoding a key regulator of phosphatidylcholine metabolism, cause spondylometaphyseal dysplasia with cone-rod dystrophy. Am. J. Hum. Genet. 94, 105–112. doi:10.1016/j.ajhg.2013.11.018

Hotamisligil, G.S., 2017. Inflammation, metaflammation and immunometabolic disorders. Nature 542, 177–185. doi:10.1038/nature21363

Hou, N.S., Gutschmidt, A., Choi, D.Y., Pather, K., Shi, X., Watts, J.L., Hoppe, T., Taubert, S., 2014. Activation of the endoplasmic reticulum unfolded protein response by lipid disequilibrium without disturbed proteostasis in vivo. Proc. Natl. Acad. Sci. U.S.A. 111, E2271–80. doi:10.1073/pnas.1318262111

Jackowski, S., Xu, X.X., Rock, C.O., 1997. Phosphatidylcholine signaling in response to CSF-1. Mol. Reprod. Dev. 46, 24–30. doi:10.1002/(SICI)1098-2795(199701)46:1<24::AID-MRD5>3.0.CO;2-T

Jiang, H., Li, Z., Huan, C., Jiang, X.-C., 2018. Macrophage Lysophosphatidylcholine Acyltransferase 3 Deficiency-Mediated Inflammation Is Not Sufficient to Induce Atherosclerosis in a Mouse Model. Front Cardiovasc Med 5, 192. doi:10.3389/fcvm.2018.00192

Kim, D., Pertea, G., Trapnell, C., Pimentel, H., Kelley, R., Salzberg, S.L., 2013. TopHat2: accurate alignment of transcriptomes in the presence of insertions, deletions and gene fusions. Genome Biol. 14. doi:10.1186/gb-2013-14-4-r36

Lancaster, G.I., Langley, K.G., Berglund, N.A., Kammoun, H.L., Reibe, S., Estevez, E., Weir, J., Mellett, N.A., Pernes, G., Conway, J.R.W., Lee, M.K.S., Timpson, P., Murphy, A.J., Masters, S.L., Gerondakis, S., Bartonicek, N., Kaczorowski, D.C., Dinger, M.E., Meikle, P.J., Bond, P.J., Febbraio, M.A., 2018. Evidence that TLR4 Is Not a Receptor for Saturated Fatty Acids but Mediates Lipid-Induced Inflammation by Reprogramming Macrophage Metabolism. Cell Metab. 27, 1096–1110.e5. doi:10.1016/j.cmet.2018.03.014

Morgantini, C., Jager, J., Li, X., Levi, L., Azzimato, V., Sulen, A., Barreby, E., Xu, C., Tencerova, M., Näslund, E., Kumar, C., Verdeguer, F., Straniero, S., Hultenby, K., Björkström, N.K., Ellis, E., Rydén, M., Kutter, C., Hurrell, T., Lauschke, V.M., Boucher, J., Tomčala, A., Krejčová, G., Bajgar, A., Aouadi, M., 2019. Liver macrophages regulate systemic metabolism through non-inflammatory factors. Nature Metabolism 2019 3, 1. doi:10.1038/s42255-019-0044-9

Payne, F., Lim, K., Girousse, A., Brown, R.J., Kory, N., Robbins, A., Xue, Y., Sleigh, A., Cochran, E., Adams, C., Dev Borman, A., Russel-Jones, D., Gorden, P., Semple, R.K., Saudek, V., O'Rahilly, S., Walther, T.C., Barroso, I., Savage, D.B., 2014. Mutations disrupting the Kennedy phosphatidylcholine pathway in humans with congenital lipodystrophy and fatty liver disease. Proc. Natl. Acad. Sci. U.S.A. 111, 8901–8906. doi:10.1073/pnas.1408523111

Prieur, X., Mok, C.Y.L., Velagapudi, V.R., Núñez, V., Fuentes, L., Montaner, D., Ishikawa, K., Camacho, A., Barbarroja, N., O'Rahilly, S., Sethi, J.K., Dopazo, J., Orešič, M., Ricote, M., Vidal-Puig, A., 2011. Differential lipid partitioning between adipocytes and tissue macrophages modulates macrophage lipotoxicity and M2/M1 polarization in obese mice. Diabetes 60, 797–809. doi:10.2337/db10-0705

Ridgway, N.D., Lagace, T.A., 2003. Regulation of the CDP-choline pathway by sterol regulatory element binding proteins involves transcriptional and post-transcriptional mechanisms. Biochem. J. 372, 811–819. doi:10.1042/BJ20030252

Robblee, M.M., Kim, C.C., Abate, J.P., Valdearcos, M., Sandlund, K.L.M., Shenoy, M.K., Volmer, R., Iwawaki, T., Koliwad, S.K., 2016. Saturated Fatty Acids Engage an IRE1α-Dependent Pathway to Activate the NLRP3 Inflammasome in Myeloid Cells. Cell Reports 14, 2611–2623. doi:10.1016/j.celrep.2016.02.053

Robinson, M.D., McCarthy, D.J., Smyth, G.K., 2010. edgeR: a Bioconductor package for differential expression analysis of digital gene expression data. Bioinformatics 26, 139–140. doi:10.1093/bioinformatics/btp616

Rong, X., Albert, C.J., Hong, C., Duerr, M.A., Chamberlain, B.T., Tarling, E.J., Ito, A., Gao, J., Wang, B., Edwards, P.A., Jung, M.E., Ford, D.A., Tontonoz, P., 2013. LXRs regulate ER stress and inflammation through dynamic modulation of membrane phospholipid composition. Cell Metab. 18, 685–697. doi:10.1016/j.cmet.2013.10.002

Sanchez-Lopez, E., Zhong, Z., Stubelius, A., Sweeney, S.R., Booshehri, L.M., Antonucci, L., Liu-Bryan, R., Lodi, A., Terkeltaub, R., Lacal, J.C., Murphy, A.N., Hoffman, H.M., Tiziani, S., Guma, M., Karin, M., 2019. Choline Uptake and Metabolism Modulate Macrophage IL-1β and IL-18 Production. Cell Metab. 1–29. doi:10.1016/j.cmet.2019.03.011

Shan, B., Wang, X., Wu, Y., Xu, C., Xia, Z., Dai, J., Shao, M., Zhao, F., He, S., Yang, L., Zhang, M., Nan, F., Li, J., Liu, J., Liu, J., Jia, W., Qiu, Y., Song, B., Han, J.-D.J., Rui, L., Duan, S.-Z., Liu, Y., 2017. The metabolic ER stress sensor IRE1α suppresses alternative activation of macrophages and impairs energy expenditure in obesity. Nature Immunology 18, 519–529. doi:10.1038/ni.3709

Shindou, H., Hishikawa, D., Harayama, T., Eto, M., Shimizu, T., 2013. Generation of membrane diversity by lysophospholipid acyltransferases. J. Biochem. 154, 21–28. doi:10.1093/jb/mvt048

Snider, S.A., Margison, K.D., Ghorbani, P., LeBlond, N.D., O'Dwyer, C., Nunes, J.R.C., Nguyen, T., Xu, H., Bennett, S.A.L., Fullerton, M.D., 2018. Choline transport links macrophage phospholipid metabolism and inflammation. Journal of Biological Chemistry 293, 11600–11611. doi:10.1074/jbc.RA118.003180

Suzuki, T., Gao, J., Ishigaki, Y., Kondo, K., Sawada, S., Izumi, T., Uno, K., Kaneko, K., Tsukita, S., Takahashi, K., Asao, A., Ishii, N., Imai, J., Yamada, T., Oyadomari, S., Katagiri, H., 2017. ER Stress Protein CHOP Mediates Insulin Resistance by Modulating Adipose Tissue Macrophage Polarity. CellReports 18, 2045–2057. doi:10.1016/j.celrep.2017.01.076

Tian, Y., Pate, C., Andreolotti, A., Wang, L., Tuomanen, E., Boyd, K., Claro, E., Jackowski, S., 2008. Cytokine secretion requires phosphatidylcholine synthesis. The Journal of Cell Biology 181, 945–957. doi:10.1083/jcb.200706152

Virtue, S., Masoodi, M., de Weijer, B.A.M., van Eijk, M., Mok, C.Y.L., Eiden, M., Dale, M., Pirraco, A., Serlie, M.J., Griffin, J.L., Vidal-Puig, A., 2015. Prostaglandin profiling reveals a role for haematopoietic prostaglandin D synthase in adipose tissue macrophage polarisation in mice and humans. Int J Obes (Lond) 39, 1151–1160. doi:10.1038/ijo.2015.34

Virtue, S., Vidal-Puig, A., 2010. Adipose tissue expandability, lipotoxicity and the Metabolic Syndrome--an allostatic perspective. Biochim. Biophys. Acta 1801, 338–349. doi:10.1016/j.bbalip.2009.12.006

Volmer, R., van der Ploeg, K., Ron, D., 2013. Membrane lipid saturation activates endoplasmic reticulum unfolded protein response transducers through their transmembrane domains. Proc. Natl. Acad. Sci. U.S.A. 110, 4628–4633. doi:10.1073/pnas.1217611110

Wei, X., Song, H., Yin, L., Rizzo, M.G., Sidhu, R., Covey, D.F., Ory, D.S., Semenkovich, C.F., 2016. Fatty acid synthesis configures the plasma membrane for inflammation in diabetes. Nature 539, 294–298. doi:10.1038/nature20117

Yamamoto, G.L., Baratela, W.A.R., Almeida, T.F., Lazar, M., Afonso, C.L., Oyamada, M.K., Suzuki, L., Oliveira, L.A.N., Ramos, E.S., Kim, C.A., Passos-Bueno, M.R., Bertola, D.R., 2014. Mutations in PCYT1A cause spondylometaphyseal dysplasia with cone-rod dystrophy. Am. J. Hum. Genet. 94, 113–119. doi:10.1016/j.ajhg.2013.11.022

Yang, X., Sheng, W., Sun, G.Y., Lee, J.C.-M., 2011. Effects of fatty acid unsaturation numbers on membrane fluidity and α-secretase-dependent amyloid precursor protein processing. Neurochem. Int. 58, 321–329. doi:10.1016/j.neuint.2010.12.004

Zhang, D., Tang, W., Yao, P.M., Yang, C., Xie, B., Jackowski, S., Tabas, I., 2000. Macrophages deficient in CTP:Phosphocholine cytidylyltransferase-alpha are viable under normal culture conditions but are highly susceptible to free cholesterol-induced death. Molecular genetic evidence that the induction of phosphatidylcholine biosynthesis in free cholesterol-loaded macrophages is an adaptive response. Journal of Biological Chemistry 275, 35368–35376. doi:10.1074/jbc.M007099200

Table S1. Biological processes increased in ob/ob compared to WT ATMs at week 16 and no change at week 5, ranked in ascending order of adjusted p value.

name	OB vs WT log.odds.ratio	OB vs WT adjusted.p.value	GO ID
RNA localization	0.109695705	6.08E-06	GO:0006403
microtubule cytoskeleton organization	0.093090767	6.50E-06	GO:0000226
chromatin assembly or disassembly	0.072715827	1.00E-05	GO:0006333
microtubule-based movement	0.090059298	2.33E-05	GO:0007018
microtubule organizing center organization	0.146245681	2.61E-05	GO:0031023
mRNA transport	0.109808548	3.59E-05	GO:0051028
regulation of DNA replication	0.138664509	4.54E-05	GO:0006275
centrosome organization	0.144335312	8.12E-05	GO:0051297
nucleobase, nucleoside, nucleotide and nucleic acid transport	0.099854207	0.000111184	GO:0015931
mRNA processing	0.0578393	0.000167041	GO:0006397
mRNA metabolic process	0.054040069	0.000340716	GO:0016071
regulation of DNA metabolic process	0.096223508	0.000421682	GO:0051052
nuclear export	0.114899289	0.000538998	GO:0051168
ER to Golgi vesicle-mediated transport	0.123039145	0.000781143	GO:0006888
sphingolipid metabolic process	0.100679526	0.000805755	GO:0006665
cytoskeleton-dependent intracellular transport	0.076563482	0.00088951	GO:0030705
mitochondrial transport	0.100785069	0.000903336	GO:0006839
negative regulation of adaptive immune response	0.141384187	0.000996114	GO:0002820
negative regulation of adaptive immune response based on somatic recombination of immune receptors built from immunoglobulin superfamily domains	0.141384187	0.000996114	GO:0002823
spindle organization	0.136044423	0.000996578	GO:0007051
proteasomal protein catabolic process	0.116160699	0.001202692	GO:0010498
proteasomal ubiquitin-dependent protein catabolic process	0.116160699	0.001202692	GO:0043161
tetrapyrrole metabolic process	0.118690789	0.001216214	GO:0033013
negative regulation of leukocyte mediated immunity	0.138596463	0.001265756	GO:0002704
negative regulation of lymphocyte mediated immunity	0.138596463	0.001265756	GO:0002707
porphyrin metabolic process	0.118893495	0.001478977	GO:0006778
pigment metabolic process	0.10813916	0.001521217	GO:0042440
centrosome duplication	0.150989536	0.001774733	GO:0051298
regulation of microtubule-based process	0.103843338	0.002239439	GO:0032886
membrane lipid metabolic process	0.063257735	0.002637924	GO:0006643
B cell homeostasis	0.128008324	0.002648853	GO:0001782
positive regulation of endocytosis	0.12047554	0.002907785	GO:0045807
regulation of phagocytosis	0.128076246	0.003712153	GO:0050764
negative regulation of immune effector process	0.124974473	0.004112746	GO:0002698
posttranscriptional regulation of gene expression	0.075584143	0.004112746	GO:0010608
negative regulation of immune response	0.118078381	0.00413245	GO:0050777
protein import into nucleus, docking	0.132229562	0.004191572	GO:0000059

phagocytosis	0.101446635	0.00503594	GO:0006909
cellular lipid catabolic process	0.093169711	0.00503594	GO:0044242
myeloid leukocyte activation	0.105316074	0.006950655	GO:0002274
regulation of mitosis	0.106515089	0.007362457	GO:0007088
cofactor catabolic process	0.11107813	0.007622515	GO:0051187
positive regulation of phagocytosis	0.128128292	0.007785139	GO:0050766
natural killer cell mediated immunity	0.119540819	0.008671944	GO:0002228
natural killer cell mediated cytotoxicity	0.119540819	0.008671944	GO:0042267
RNA splicing	0.051881202	0.008977949	GO:0008380
protein ubiquitination	0.079124981	0.00903524	GO:0016567
phospholipid biosynthetic process	0.084888604	0.009600299	GO:0008654
protein export from nucleus	0.130373098	0.009827841	GO:0006611
regulation of mitotic metaphase/anaphase transition	0.140486196	0.010926482	GO:0030071
protein modification by small protein conjugation	0.07415241	0.012375254	GO:0032446
establishment or maintenance of chromatin architecture	0.04324993	0.012884899	GO:0006325
membrane lipid biosynthetic process	0.07747481	0.013692795	GO:0046467
amino acid transport	0.082876543	0.017506793	GO:0006865
homophilic cell adhesion	0.072883396	0.020657461	GO:0007156
meiosis I	0.1025323	0.022072268	GO:0007127
sterol transport	0.117152176	0.025155824	GO:0015918
cholesterol transport	0.117152176	0.025155824	GO:0030301
glycerophospholipid metabolic process	0.077396853	0.025221219	GO:0006650
coenzyme catabolic process	0.107467379	0.031451225	GO:0009109
macroautophagy	0.124851577	0.03246804	GO:0016236
immune response-regulating cell surface receptor signaling pathway	0.092804257	0.035270204	GO:0002768
tricarboxylic acid cycle	0.114235727	0.035778842	GO:0006099
posttranscriptional gene silencing	0.125397712	0.041310187	GO:0016441
posttranscriptional gene silencing by RNA	0.125397712	0.041310187	GO:0035194
regulation of endocytosis	0.091158719	0.044384454	GO:0030100
regulation of translation	0.076317448	0.044950188	GO:0006417
embryonic cleavage	0.136020547	0.046564678	GO:0040016
immune response-activating signal transduction	0.089300606	0.04715384	GO:0002757
acetyl-CoA catabolic process	0.111487385	0.048713909	GO:0046356
DNA damage response, signal transduction	0.086685282	0.04960336	GO:0042770

1
2

Table S2. Differentially regulated GO biological processes in eWAT isolated from ob/ob BMT Pcyt1a$^{fl/fl}$ and Pcyt1a$^{fl/fl}$ LysM-Cre mice, ranked in ascending order of p value.

Pathway/term	Direction	statistic	p.value
insulin receptor signaling pathway	UP	3.130495169	0.000582751
circadian rhythm	UP	3.130495169	0.000582751
cellular response to growth factor stimulus	UP	2.874944543	0.002331002
positive regulation of phosphatidylinositol 3-kinase signaling	DOWN	-2.874944543	0.002331002
cellular response to zinc ion	UP	2.74716923	0.004079254
extracellular matrix constituent secretion	UP	2.74716923	0.004079254
positive regulation of transcription from RNA polymerase II promoter in response to endoplasmic reticulum stress	UP	2.74716923	0.004079254
negative regulation of endoplasmic reticulum stress-induced intrinsic apoptotic signaling pathway	UP	2.74716923	0.004079254
regulation of necrotic cell death	DOWN	-2.74716923	0.004079254
cellular response to insulin stimulus	UP	2.619393917	0.006993007
mRNA transcription from RNA polymerase II promoter	UP	2.619393917	0.006993007
negative regulation of BMP signaling pathway	UP	2.619393917	0.006993007
protein processing	DOWN	-2.619393917	0.006993007
brain-derived neurotrophic factor receptor signaling pathway	UP	2.491618604	0.011072261
regulation of GTPase activity	UP	2.491618604	0.011072261
intracellular signal transduction	UP	2.491618604	0.011072261
IRES-dependent translational initiation	UP	2.491618604	0.011072261
negative regulation of translational initiation	UP	2.491618604	0.011072261
inner ear development	DOWN	-2.491618604	0.011072261
positive regulation of fever generation	DOWN	-2.491618604	0.011072261
positive regulation of tumor necrosis factor-mediated signaling pathway	DOWN	-2.491618604	0.011072261
positive regulation of I-kappaB phosphorylation	DOWN	-2.491618604	0.011072261
regulation of JNK cascade	DOWN	-2.491618604	0.011072261
cellular protein complex assembly	DOWN	-2.491618604	0.011072261
regulation of protein phosphorylation	DOWN	-2.491618604	0.011072261
negative regulation of cytokine secretion involved in immune response	DOWN	-2.491618604	0.011072261
glomerulus vasculature development	DOWN	-2.491618604	0.011072261
regulation of macrophage migration inhibitory factor signaling pathway	DOWN	-2.491618604	0.011072261
regulation of tumor necrosis factor production	DOWN	-2.491618604	0.011072261
negative regulation of vascular permeability	DOWN	-2.491618604	0.011072261
cell-substrate adhesion	DOWN	-2.491618604	0.011072261
negative regulation of protein import into nucleus	DOWN	-2.491618604	0.011072261
regulation of protein binding	DOWN	-2.491618604	0.011072261
negative regulation of protein phosphorylation	DOWN	-2.491618604	0.011072261
negative regulation of cell-substrate adhesion	DOWN	-2.491618604	0.011072261
fructose 6-phosphate metabolic process	UP	2.491618604	0.011072261
negative regulation of insulin secretion	UP	2.491618604	0.011072261
glycolytic process through fructose-6-phosphate	UP	2.491618604	0.011072261
response to glucose	UP	2.491618604	0.011072261
malonyl-CoA catabolic process	UP	2.491618604	0.011072261
positive regulation of fatty acid oxidation	UP	2.491618604	0.011072261
regulation of establishment or maintenance of cell polarity	DOWN	-2.491618604	0.011072261
multicellular organism growth	DOWN	-2.491618604	0.011072261

prostate gland growth	DOWN	-2.491618604	0.011072261
insulin-like growth factor receptor signaling pathway	DOWN	-2.491618604	0.011072261
chondroitin sulfate proteoglycan biosynthetic process	DOWN	-2.491618604	0.011072261
antigen receptor-mediated signaling pathway	UP	2.491618604	0.011072261
neutrophil apoptotic process	UP	2.491618604	0.011072261
negative regulation of chemokine biosynthetic process	UP	2.491618604	0.011072261
negative regulation of hormone secretion	UP	2.491618604	0.011072261
positive regulation of T-helper 2 cell differentiation	UP	2.491618604	0.011072261
branching involved in salivary gland morphogenesis	UP	2.491618604	0.011072261
cellular response to interleukin-1	UP	2.491618604	0.011072261
cellular response to tumor necrosis factor	UP	2.491618604	0.011072261
positive regulation of neuron projection development	UP	2.363843291	0.017482518
nerve growth factor signaling pathway	UP	2.363843291	0.017482518
cellular response to nerve growth factor stimulus	UP	2.363843291	0.017482518
positive regulation of synapse assembly	UP	2.363843291	0.017482518
nervous system development	UP	2.363843291	0.017482518
negative regulation of anoikis	UP	2.363843291	0.017482518
cellular response to organic substance	DOWN	-2.363843291	0.017482518
cellular response to amino acid starvation	UP	2.363843291	0.017482518
regulation of microtubule-based movement	UP	2.363843291	0.017482518
extracellular matrix organization	DOWN	-2.363843291	0.017482518
interleukin-6-mediated signaling pathway	UP	2.363843291	0.017482518
inositol trisphosphate biosynthetic process	DOWN	-2.363843291	0.017482518
tumor necrosis factor-mediated signaling pathway	DOWN	-2.363843291	0.017482518
cellular extravasation	DOWN	-2.363843291	0.017482518
positive regulation of translational initiation by iron	DOWN	-2.363843291	0.017482518
regulation of branching involved in salivary gland morphogenesis	DOWN	-2.363843291	0.017482518
negative regulation of alkaline phosphatase activity	DOWN	-2.363843291	0.017482518
negative regulation of glucose import	DOWN	-2.363843291	0.017482518
regulation of protein secretion	DOWN	-2.363843291	0.017482518
regulation of reactive oxygen species metabolic process	DOWN	-2.363843291	0.017482518
defense response to bacterium	DOWN	-2.363843291	0.017482518
negative regulation of NF-kappaB transcription factor activity	DOWN	-2.363843291	0.017482518
hydrogen peroxide catabolic process	DOWN	-2.363843291	0.017482518
protein acetylation	UP	2.363843291	0.017482518
positive regulation of transcription from RNA polymerase II promoter involved in unfolded protein response	UP	2.363843291	0.017482518
protein stabilization	UP	2.363843291	0.017482518
release of sequestered calcium ion into cytosol by sarcoplasmic reticulum	UP	2.363843291	0.017482518
response to caffeine	UP	2.363843291	0.017482518
cellular response to caffeine	UP	2.363843291	0.017482518
growth hormone secretion	UP	2.363843291	0.017482518
positive regulation of tyrosine phosphorylation of Stat5 protein	UP	2.363843291	0.017482518
programmed necrotic cell death	DOWN	-2.363843291	0.017482518
positive regulation of innate immune response	DOWN	-2.363843291	0.017482518
regulation of blood pressure	DOWN	-2.363843291	0.017482518
response to organic substance	DOWN	-2.236067978	0.026223776
cellular response to lipopolysaccharide	UP	2.236067978	0.026223776
epidermal growth factor receptor signaling pathway	UP	2.236067978	0.026223776
regulation of multicellular organism growth	UP	2.236067978	0.026223776

JAK-STAT cascade	UP	2.236067978	0.026223776
positive regulation of interleukin-6 production	DOWN	-2.236067978	0.026223776
organ induction	UP	2.236067978	0.026223776
positive regulation of epithelial cell proliferation	UP	2.236067978	0.026223776
leukocyte migration	DOWN	-2.236067978	0.026223776
positive regulation of JNK cascade	DOWN	-2.236067978	0.026223776
response to molecule of bacterial origin	DOWN	-2.236067978	0.026223776
positive regulation of protein kinase B signaling	DOWN	-2.236067978	0.026223776
positive regulation of cerebellar granule cell precursor proliferation	DOWN	-2.236067978	0.026223776
glucose homeostasis	UP	2.236067978	0.026223776
activation of cysteine-type endopeptidase activity involved in apoptotic process by cytochrome c	DOWN	-2.236067978	0.026223776
positive regulation of extrinsic apoptotic signaling pathway in absence of ligand	DOWN	-2.236067978	0.026223776
positive regulation of axon regeneration	UP	2.236067978	0.026223776
early endosome to late endosome transport	DOWN	-2.236067978	0.026223776
muscle fiber development	DOWN	-2.236067978	0.026223776
collagen catabolic process	DOWN	-2.236067978	0.026223776
B cell receptor signaling pathway	UP	2.108292665	0.037878788
platelet-derived growth factor receptor-alpha signaling pathway	DOWN	-2.108292665	0.037878788
positive regulation of chemotaxis	DOWN	-2.108292665	0.037878788
positive regulation of MAP kinase activity	DOWN	-2.108292665	0.037878788
apoptotic process	DOWN	-2.108292665	0.037878788
vesicle targeting	DOWN	-2.108292665	0.037878788
liver regeneration	DOWN	-2.108292665	0.037878788
embryo implantation	DOWN	-2.108292665	0.037878788
proteolysis	DOWN	-2.108292665	0.037878788
angiogenesis	UP	2.108292665	0.037878788
activation of MAPK activity	UP	2.108292665	0.037878788
cellular response to glucose stimulus	DOWN	-2.108292665	0.037878788
brown fat cell differentiation	UP	2.108292665	0.037878788
negative regulation of fibroblast proliferation	UP	2.108292665	0.037878788
white fat cell differentiation	UP	2.108292665	0.037878788
positive regulation of establishment of protein localization to plasma membrane	DOWN	-2.108292665	0.037878788
protein localization to cell surface	DOWN	-2.108292665	0.037878788
embryonic hemopoiesis	UP	2.108292665	0.037878788
movement of cell or subcellular component	UP	2.108292665	0.037878788

1

Table S3. Sequences of primers used in this publication.

FAM/TAMRA reporter and quencher detection system was used for genes with indicated probe sequences, and SYBR was used for the remaining genes.

Gene	Forward primer (5'-3')	Reverse primer (5'-3')	Probe (5'-3')
18s	CGGCTACCACATCCAAGGAA	GCTGGAATTACCGCGGCT	GAGGGCAAGTCTGGTGCCAG
36b4	AGATGCAGCAGATCCGCAT	GTTCTTGCCCATCAGCACC	
Actb (human)	TGAGATGCGTTGTTACAGGAAGTC	GACTGGGCCATTCTCCTTAGAGA	CTTGCCATCCTAAAAGCCACCCCACTT
Arg1	CTCCAAGCCAAAGTCCTTAGAG	AGGAGCTGTCATTAGGGACATC	
Atf4	ATGATGGCTTGGCCAGTG	CCATTTTCTCCAACATCCAATC	
B2m (human)	CGCTCCGTGGCCTTAGC	AATCTTTGGAGTACGCTGGATAGC	TGCTCGCGCTACTCTCTCTTTCTGGC
Hspa5	CTGAGGCGTATTTGGGAAAG	TCATGACATTCAGTCCAGCAA	
Ddit3	CCACCACACCTGAAAGCAGAA	AGGTGAAAGGCAGGGACTCA	
Elovl5	TTCGATGCGTCACTCAGTACCT	TGTCCAGGAGGAACCATCCTT	
Elovl6	TGCAGGAAAACTGGAAGAAGTCT	ATGCCGACCACCAAAGATAAA	
Emr1	CAGATACAGCAATGCCAAGCA	GATTGTGAAGGTAGCATTCACAAGTG	
ERdj4	CACAAAGATGCCTTTTCTACCG	TTAAACTTTTCAGCTTAATGACGTG	
Fads1	TGCACCCCCTCTTCTTCGCC	AGGCTGGGGGTCCGATGAGG	
Fads2	AGCCCTGGTTTTCCTCAACT	GTTGTGACGTGGCATAGTGG	
Fasn	GCCCAGACAGAGAAGAGGCA	CTGACTCGGGCAACTTCCC	GGAGGAGGTGGTGATAGCCGGTATGTC
Fatp1	CGTTTCGATGGTTATGTTAGTGACA	CATCACTAGCACGTCACCTGAGA	
Gapdh (human)	CCAGGTGGTCTCCTCTGACTTC	TCATACCAGGAAATGAGCTTGACA	ACAGCGACACCCACTCCTCCACCTT
Glut4	ACTCATTCTTGGACGGTTCCTC	CACCCCGAAGATGAGTGGG	TGGCGCCTACTCAGGGCTAACATCA
Il10	CAGAGCCACATGCTCCTAGA	TGTCCAGCTGGTCCTTTGTT	
Insig1	GCGCTGTATTGCCGTGTTC	ACAGCTGGACATTATTGGCAAA	CATCAACCACGCCAGTGCCA
Itgam	CAGACAGGAAGTAGCAGCTCCT	CTGGTCATGTTGATGAAGGTGCT	
Itgax	GGCTATCAAGCATGTCATAACAGAAC	CCCCTTGTTTTCTCCCATCAG	

Mgl1	AGGTCCCTGTCATGCTTCTG	GCTGCTGGTGATCCTCTTGT	
Mrc1	GCATGGGTTTTACTGCTACTTGATT	CAGGAATGCTTGTTCATATCTGTCTT	
Pcyt1a	TCTGCAGGGAGCGATGATG	TGTGGAGATACCTTCTGTCCTCTGT	TATAAGCACATCAAGGACGCAGGCATGTT
Pcyt1a (human)	Commercial assay (Hs00192339_m1, Thermofisher)		
Pcyt1b	CAGTGCCAAGCACCTCATGA	GGCCTATCAACTGGTGTTCCTAA	
Polr2a (human)	GCTATAAGGTGGAACGGCACAT	ACCCGATGCCCCATCAT	AACCGGCAGCCAACTCTGCACAA
Scd1	CTTGCGGATCTTCCTTATCATT	GATCTCGGGCCCATTCG	ACCATGGCGTTCCAGAATGACGTGT
Scd2	TGGTTTCCATGGGAGCTG	TTGATGTGCCAGCGGTACT	
Srebf1	GCCATGGATTGCACATTTGA	GGCCCGGGAAGTCACTG	GACATGCTCCAGCTCATCAACAACCAAG
Tbp	CAAACCCAGAATTGTTCTCCTT	ATGTGGTCTTCCTGAATCCCT	
Tnf	CATCTTCTCAAAATTCGAGTGACAA	TGGGAGTAGACAAGGTACAACCC	CACGTCGTAGCAAACCACCAAGTGGA
Xbp1 spliced	AGCTTTTACGGGAGAAAACTCA	GCCTGCACCTGCTGCG	
Xbp1 total	ACACGCTTGGGAATGGACAC	CCATGGGAAGATGTTCTGGG	

1